Olig2 and Hes regulatory dynamics during motor neuron differentiation revealed by single cell transcriptomics

Andreas Sagner*,[1], Zachary Gaber*,[2], Julien Delile*,[1], Jennifer H. Kong[2], David L. Rousso[2], Caroline A. Pearson[2], Steven E. Weicksel[3], S. Neda Mousavy Gharavy[1], James Briscoe§,[1], Bennett G. Novitch§,[2,3]

*These authors contributed equally

[1]The Francis Crick Institute, 1 Midland Road, London NW1 1AT, UK

[2]Department of Neurobiology, Eli and Edythe Broad Center for Regenerative Medicine and Stem Cell Research, David Geffen School of Medicine at UCLA, 610 Charles E Young Dr East, TLSB 3024, Los Angeles, California 90095, USA

[3]Department of Cell and Developmental Biology, University of Michigan Medical School, Ann Arbor, MI 48109

§ Correspondence to either J. Briscoe or B. Novitch

ABSTRACT

During tissue development, multipotent progenitors differentiate into specific cell types in characteristic spatial and temporal patterns. We address the mechanism linking progenitor identity and differentiation rate in the neural tube, where motor neuron (MN) progenitors differentiate more rapidly than other progenitors. Using single cell transcriptomics, we define the transcriptional changes associated with the transition of neural progenitors into MNs. Reconstruction of gene expression dynamics from these data indicate a pivotal role for the MN determinant Olig2 just prior to MN differentiation. Olig2 represses expression of the Notch signaling pathway effectors Hes1 and Hes5. Olig2 repression of Hes5 appears to be direct, via a conserved regulatory element within the Hes5 locus that restricts expression from MN progenitors. These findings reveal a tight coupling between the regulatory networks that control patterning and neuronal differentiation, and demonstrate how Olig2 acts as the developmental pacemaker coordinating the spatial and temporal pattern of MN generation.

INTRODUCTION

The orderly development of embryonic tissues relies on gene regulatory networks that control patterns of gene expression, tissue growth and cell differentiation (Davidson 2010; Stathopoulos and Levine 2005). Genetic and molecular studies have identified many of the constituents of these networks and begun to define the regulatory hierarchy between them. Nevertheless, how cell fate assignment is coordinated with proliferation and differentiation remains poorly understood.

An experimentally well-characterised tissue that exemplifies this problem is the vertebrate spinal cord. In ventral regions of the developing spinal cord proliferating progenitors are exposed to a gradient of Sonic Hedgehog (Shh) signalling that controls the expression of a set of homeodomain and basic helix-loop-helix (bHLH) transcription factors (TFs) (Briscoe et al. 2000; Ribes and Briscoe 2009; Briscoe and Ericson 1999). These TFs form a gene regulatory network that progressively allocates progenitor identity, dividing the spinal cord into molecularly discrete domains arrayed along the dorsal-ventral axis (Balaskas et al. 2012; Cohen et al. 2013). This combinatorial transcriptional code determines the subtype identity of the post-mitotic neurons generated by progenitors in each domain, thereby controlling the position at which motor neurons (MNs) and interneurons emerge (Briscoe et al. 2000; Jessell 2000; Lee and Pfaff 2001; Alaynick et al. 2011).

Among the first neurons to differentiate in the ventral spinal cord are MNs. In mouse and chick, these are formed over a 2 to 3-day period (Kicheva et al. 2014). During this time, most if not all MN progenitors exit the cell cycle and differentiate, whereas the adjacent progenitor domains that give rise to interneurons continue to divide and consequently differentiate at a much slower pace (Kicheva et al. 2014; Ericson et al. 1992). These differences in differentiation rate play an important role in the elaboration of spinal cord pattern and ensure appropriate numbers of MNs are generated. This raises the question of how the regulatory mechanisms defining MN progenitors prime these cells to differentiate rapidly.

The induction and differentiation of MNs is characterized by a series of gene expression changes. Initially, Shh signaling induces the bHLH protein Olig2, resulting in the repression of the homeodomain protein Irx3 and bHLH protein Bhlhb5, normally expressed in neural progenitors (NPs) dorsal to MNs (Novitch et al. 2001; Zhou and Anderson 2002; Lu et al. 2002; Skaggs et al. 2011). Ectopic expression of Olig2 represses both Irx3 and Bhlhb5, resulting in ectopic MN production (Novitch et al. 2001; Mizuguchi et al. 2001). Conversely, in the absence of *Olig2*, MN generation fails and instead Irx3 and

Bhlhb5 expression is maintained and NPs differentiate into ventral interneurons (Zhou and Anderson 2002; Lu et al. 2002; Takebayashi et al. 2002; Skaggs et al. 2011).

Olig2 also accelerates cell cycle exit (Novitch et al. 2001), while the absence of Olig2 results in a characteristically slower tempo of neuronal differentiation (Zhou and Anderson 2002). Olig2 promotes the expression of the bHLH TF Ngn2 and ectopic expression of Ngn2 causes progenitor cells to exit the cell cycle to differentiate prematurely into neurons (Novitch et al. 2001; Scardigli et al. 2001; Mizuguchi et al. 2001; Bertrand et al. 2002; Lu et al. 2000; Sugimori et al. 2007; Lacomme et al. 2012). Previous studies have shown that Olig2 acts as a transcriptional repressor to promote Ngn2 expression and to specify MN identity (Novitch et al. 2001; Mizuguchi et al. 2001). This implies that Olig2 promotes Ngn2 expression by negatively regulating the expression of Ngn2 repressors. Potential candidates are members of the Hairy/Enhancer of Split (Hes) family of transcriptional repressors, which act downstream of the Notch signaling pathway to prevent neuronal differentiation and maintain progenitors in a dividing, undifferentiated state (Ohtsuka et al. 1999; Shimojo et al. 2011; Kageyama et al. 2007). While much is known about how activation of the Notch pathway promotes *Hes* gene expression, less is known about the mechanisms by which *Hes* genes are suppressed to enable neuronal differentiation to proceed in a temporally and spatially organized manner. Specifically, how Olig2 expression both specifies MN progenitor identity and regulates their rate of differentiation is not understood.

Single cell RNA sequencing is emerging as a novel and powerful technology to identify distinct cell types in complex mixtures and to define developmental trajectories during differentiation (Scialdone et al. 2016; Treutlein et al. 2016; Setty et al. 2016; Trapnell et al. 2014; Shin et al. 2015). Here we take advantage of an *in vitro* model that allows the generation of ventral spinal cord cell types from embryonic stem cells (ESCs) to perform single cell transcriptome analysis of developing NPs (Gouti et al. 2014). We use these data to reconstruct and validate the differentiation trajectory of MN progenitors. This provided much greater temporal resolution than previously available and identified a sequence of distinct phases in MN differentiation, including two distinct Olig2 expression states. An initial Olig2^{LOW} state, during which Hes1 expression decreases and Olig2 is coexpressed with Hes5, and a subsequent Olig2^{HIGH} state in which high levels of Olig2 promote differentiation by repressing Hes5, thereby indirectly inducing Ngn2. We validate this two-phase model using quantitative image analysis of a fluorescent Olig2 reporter and provide *in vitro* and *in vivo* evidence that Olig2 acts directly on Hes genes to promote cell cycle exit and neurogenesis in the pMN domain. Together the data provide a comprehensive view of the regulatory network that controls the specification of MN progenitors and identified a mechanism coordinating the specification of positional identity with differentiation.

RESULTS

In vitro generation of Motor Neuron and V3 progenitors

To define the sequence of events that lead to the generation of somatic MNs, we took advantage of ESCs, which can be directed to differentiate into spinal NPs *in vitro* (Gouti et al. 2014). This method relies on the exposure of ESCs, cultured as a monolayer, to a brief pulse of Wnt signalling prior to neural induction (Fig. 1A). This induces the caudalizing TFs Cdx1,2,4 (Gouti et al. 2014). Subsequently, removal of Wnt signalling and exposure to retinoic acid (RA) results in the generation of NPs expressing initially *Hoxb1* and later *Hoxb9* (Figure 1-figure supplement 1A). These differentiate into *Hoxc6*-positive neurons, characteristic of forelimb level spinal cord MNs (Figure 1-figure supplement 1A,B)) (Dasen et al. 2003; Philippidou and Dasen 2013; Stifani 2014; Gouti et al. 2014). Exposure of these NPs to Shh signalling agonist SAG induces the expression of genes expressed in the ventral spinal cord, including progenitor markers such as Olig2 and Nkx2.2, and the induction of MNs expressing post-mitotic markers including Islet1 (Isl1), Mnx1 and neuronal class III beta-tubulin (Tubb3) (Fig. 1B,C and Figure 1-figure supplement 1B,C).

In vivo NPs respond to Shh signalling by transitioning through a succession of progressively more ventral gene expression states (Chamberlain et al. 2008; Dessaud et al. 2010; Balaskas et al. 2012; Jeong and McMahon 2005). We tested whether a similar sequence was observed *in vitro*. At Day 3.5 (D3.5), 12h after the cessation of Wnt signalling and addition of SAG, cells were expressing *Sox1*, *Pax6* and *Irx3*, this is consistent with the acquisition of NP identity (Fig. 1B,D). The absence of ventral markers at this stage indicates that these NPs initially adopt a dorsal/intermediate positional identity (Jeong and McMahon 2005; Dessaud et al. 2010). By D4, the expression of *Pax6* and *Irx3* were maintained and *Nkx6.1*, which is expressed broadly in the ventral third of the neural tube, was induced (Fig. 1B,D). Within 12h of this time point, *Olig2* expression commenced and both *Pax6* and *Irx3* declined (Fig. 1B-D). Over the next 48h, *Pax6* and *Irx3* became further repressed, *Nkx2.2* increased and *Olig2* expression began to decline (Fig. 1B-D). This temporal sequence of gene expression is strikingly similar to that observed in the embryonic neural tube (Dessaud et al. 2010; Balaskas et al. 2012; Jeong and McMahon 2005), and suggests that between D4.5 and ~D6 MN progenitors are generated *in vitro*.

Consistent with the generation of MN progenitors *in vitro*, *Ngn2* was induced following *Olig2* (Fig. 1E) and then with a ~12h delay markers characteristic of post-mitotic MNs, including *Isl1* and *Tubb3*, were observed (Fig. 1C,E). Concomitantly, the expression of the pan NP marker *Sox1* declined (Fig. 1C,E). Taken together, these data indicate that this method of directing ESC differentiation recapitulates *in vivo* dynamics of neural tube patterning between approximately e8.5 and e10.5 and results in the production of MN progenitors and MNs characteristic of those normally found at forelimb levels.

Single cell transcriptome analysis of *in vitro* NPs

We reasoned that analysing the transcriptome of individual cells would provide insight into the transitions in gene expression associated with the differentiation of MNs and allow the construction of a detailed developmental timeline. We therefore performed single cell transcriptome analysis (RNA-seq) using the Fluidigm-C1 platform on 236 cells isolated from D4-D6 of the differentiation protocol. After applying quality filters (see Analytical Supplement) transcriptomes of 202 cells were retained for subsequent analysis (25 cells from D4, 68 cells from D5 and 109 cells from D6). To identify the cell states present in the dataset, we established a data driven analysis pipeline based on hierarchical clustering and association of gene modules with specific GO terms (see Analytical Supplement). In brief, the data were first filtered by removing genes that did not exceed a Spearman correlation of r>0.4 with at least two other genes (retaining 2287 genes). A combination of hierarchical clustering and automated selection criteria identified 22 gene modules that represent distinct patterns of gene expression across the dataset (see Analytical Supplement). Further functional characterization of these gene modules based on GO terms resulted in the identification of 10 gene modules that were sufficient to assign a cell type classification to each cell in the dataset using hierarchical clustering (Figure 2-figure supplement 1A).

Consistent with our previous finding that the spinal NPs generated by differentiation of ESCs share a developmental lineage with trunk mesoderm (Gouti et al. 2014), we observed two mesodermal cell populations in our dataset: paraxial presomitic mesoderm characterized by the expression of *Meox1* and *Foxc1*, and a vascular endothelial population expressing *Dll4* and *Cdh5* (Figure 2-figure supplement 1A). The remaining cell clusters corresponded to different stages of NPs and differentiating MNs (Fig 2A). Five gene modules were associated with these cells (comprising 306 genes). Module 1 was enriched for genes upregulated in early NPs, including the TF *Irx3*. Module 2 contained genes expressed in MN progenitors, including the ventral progenitor markers *Olig2* and *Nkx6.1,* and the neural-specific POU TF *Pou3f2* (aka Brn-2). Module 3 comprised a set of genes transiently expressed in MNs as they differentiate, such as the bHLH TFs *Ngn2*, *Neurod1*, *Neurod4* and *Hes6*, the homeodomain TFs Isl1 and Lhx3, and the Notch ligand *Dll1*. Modules 4 and 5 revealed two successive waves of neuronal gene induction. Module 4 contained genes induced early in differentiated MNs such as *Tubb3*, the RNA-binding protein *Elavl3* (aka *HuC*) and the SoxC TF *Sox4*, while Module 5 consisted of genes characteristic of more mature MNs, represented by *Chat* (*Choline acetyltransferase*) and the TFs *Isl2* and *Onecut1* (Velasco et al. 2016; Rhee et al. 2016; Thaler et al. 2004; Tanabe et al. 1998).

Whereas the five cell clusters defined by these modules represented a progressive shift of cell states from early progenitor cells to MNs, the cell cluster represented by Module 6 exhibited a divergent gene expression signature. Many genes contained in Modules 1 and 2 were downregulated but neuronal gene expression was not increased. Differential expression analysis on this population identified the glial marker *Fabp7* and the astrocyte-associated gene *Npas3* as enriched in these cells (Brunskill et al. 1999; Cahoy et al. 2008). We therefore conclude that this cluster contains gliogenic progenitors. Taken together the analysis suggests that the single cell transcriptome analysis identifies cells along the MN developmental timeline and partitions these into specific cell types from early NPs to post-mitotic neurons and glial progenitors.

We next asked whether it was possible to reconstruct the developmental timeline from the transcriptome data. For this we used the 306 genes contained in the 5 neural gene modules to visualize the developmental trajectory as a pseudotemporal ordering derived from a consensus of a large number of randomized minimum spanning trees (see Analytical Supplement). The resulting cell graph represents the predicted developmental order of cells based on their transcriptome profile and hence differentiation state (Figure 2B). Strikingly, the five previously characterized cell clusters were ordered on the cell state graphs as expected from the characterization of their gene expression profile (Fig. 2C). The graph revealed developmental trajectories originating from *Irx3* expressing early progenitors to a bipotent population of MN progenitors characterized by *Olig2* expression (Fig. 2C). These progenitors then bifurcated into MNs via the subsequent expression of *Ngn2*, *Isl1* and *Chat* and into glial progenitors characterized by *Fabp7* expression (Fig. 2C). To investigate these trajectories in more detail we focused on the developmental trajectory leading from neural progenitors to MNs. To represent changes in gene expression in an unbiased manner, we reconstructed the average gene expression program along pseudotime from the 9000 shortest paths connecting *Irx3* expressing progenitor cells to differentiated MNs on the cell state graph (starred cells in Fig. 2B, see Analytical Supplement). Each individual path was resampled to a constant length of 40 pseudotime points (Figure 2D), allowing statistical measurements along the developmental timelines. The outcome was predicted gene expression dynamics during MN differentiation

Characterization of transcriptional changes along the differentiation trajectory to motor neurons

As a first validation, we asked if the pseudotemporal ordering reproduced the temporal sequence of well characterized gene expression changes that lead to MN differentiation. The inferred trajectory correctly predicted the induction sequence of homeodomain and bHLH TFs *Irx3*, *Pax6*, *Nkx6.1*, and *Olig2* involved in ventral patterning of the spinal cord (Fig. 2E) (Dessaud et al. 2010; Jeong and McMahon 2005; Chamberlain et al. 2008). Next we focused on the transition from progenitors to MNs. As expected, this transition was associated with the transient expression of *Ngn2*, *Neurod4* and *Lhx3*, followed by the expression of MN markers including *Isl1/2*, *Tubb3* and *Chat* (Fig. 2E). Taken together, these data suggest that the pseudotemporal ordering correctly described transcriptome-wide changes in the gene expression profile along the MN developmental timeline with unprecedented resolution.

The process of cell development has been characterised as a series of metastable states defined by a relatively homogenous gene expression program connected by stereotypic transitions (Moris et al. 2016). During these transitions coordinated changes in gene expression occur, often induced in response to a change in signalling. We reasoned metastable states and transition phases should be evident in the pseudotemporal ordering. Quantifying the variation in gene expression by averaging the normalized derivative of the most dispersed genes' expression profiles identified these phases (Fig. 2D). The three metastable states in which gene expression changes were relatively modest corresponded to early neural progenitors, pMN and MNs. Linking these states were transitions characterized by an increased change in the global gene expression profile. The first transition corresponded to the switch from *Irx3* expressing intermediate progenitors to *Olig2* expressing MN progenitors. The second captured the transition of progenitors to post-mitotic neurons.

We asked whether signatures of signalling pathways driving these transitions could be identified. To this end, we examined the induction and disappearance of canonical target genes for different signalling pathways. As expected, the transition from *Irx3* to *Olig2* coincided with the induction of well-known Shh target genes *Ptch2*, *Hhip1* and *Gli1,* consistent with Shh signalling mediating this transition (Figure FIGURE 2-FIGURE SUPPLEMENT 1B). By contrast, the second transition was accompanied by a loss of Notch signalling, marked by the disappearance of *Hes1/5* and induction of markers causing or characteristic of a loss of Notch signalling, including *Numbl*, *Hes6*, *Dll1*, *Ngn2* and *Neurod4* (Figs. 2E and Figure 2-figure supplement 1C). Strikingly, the beginning of this stage coincided with peak expression levels of *Olig2* (Fig. 2E,F). This finding raised the possibility that high levels of Olig2 promote neurogenesis, potentially by directly regulating levels of Notch signalling. In summary, the characterization of changes in the transcriptional profile in pseudotime identified distinct metastable cell states and the signalling pathways associated with the transitions between these states.

In vitro and *in vivo* validation of the pseudotemporal ordering

To extend this approach and validate the predicted timeline we asked whether the data was sufficient to capture fine-grained temporal information that could be tested experimentally. Examination of the transition from *Olig2* expressing progenitors to *Isl1* expressing MNs predicted the transient expression of first *Ngn2*, then *Lhx3* and finally *Isl1*. This is consistent with *in vivo* data indicating that *Lhx3* precedes the expression of other MN markers in the spinal cord (Arber et al. 1999; Tanabe et al. 1998) and a similar sequence of gene expression has been described in an *in vitro* MN differentiation protocol based on embryoid bodies (Rhee et al. 2016; Tan et al. 2016). To confirm this sequence of events *in vitro* we assayed Olig2, Ngn2, Lhx3, and Isl1 on D6 of differentiation and quantified the levels of expression in individual nuclei (Figure 3-figure supplement 1A). Comparison of the levels of Olig2 and Isl1 in individual nuclei revealed a clear trajectory from Olig2-positive, Isl1-negative NPs to Isl1-positive, Olig2-negative MNs. Overlaying the levels of Ngn2 and Lhx3, in the same cells, revealed that both proteins are only transiently expressed along the differentiation trajectory (Figure 3-figure supplement 1B,C). To confirm the absence of Lhx3 in more mature MNs, we assayed Lhx3, Isl1 and the pan-neuronal marker Tubb3 (Figure 3-figure supplement 1D). Consistent with the pseudotemporal ordering, most Tubb3 expressing cells displayed high levels of Isl1 expression but only low levels of Lhx3, while cells with high levels of Lhx3 did not express high levels of Isl1 or Tubb3. In summary, these two observations confirm the predictions from the pseudotemporal ordering and validate the approach for predicting fine-grained changes in the transcriptional program of cells along the differentiation trajectory to MNs.

To further test the reliability of the timeline and demonstrate the validity of the approach for understanding MN differentiation dynamics, we asked if we could predict novel genes involved in MN formation. To this end, we selected genes positively correlated with *Olig2* and *Ngn2* (Figure 3-figure supplement 1E,F). One gene with a particularly strong relationship was *Zbtb18* (also known as *RP58* or *Zfp238*). Zbtb18 is a zinc-finger TF with a BTB domain. In the brain its loss causes microcephaly and decreased neuronal and increased glial differentiation (Xiang et al. 2011). Less is known about its expression pattern and role in the spinal cord, although *in situ* hybridisation analyses have suggested it is predominantly expressed in ventral progenitors (Oosterveen et al. 2013). As expected, when we assayed Zbtb18 using immunohistochemistry, it was expressed in cells that also expressed Olig2 and Ngn2 (Figure 3-figure supplement 1H-J). Consistent with this, its expression was detected *in vivo* in the pMN domain at e9.5 in cells that also expressed high levels of Olig2 and Ngn2 (Figure 3-figure supplement 1K). At e10.5, it was still predominantly expressed ventrally, although no longer confined to the pMN domain (Figure 3-figure supplement 1L). In summary, this expression pattern further validates the computationally reconstructed MN differentiation timeline.

Olig2 expression increases as cells commit to MN differentiation

The MN differentiation timeline indicated that *Olig2* expression was induced as *Irx3* was repressed, consistent with the cross repressive interactions between these two genes (Novitch et al. 2001; Mizuguchi et al. 2001; Chen et al. 2011). This transition demarcated the transition from the first to the second phase identified in the MN timeline. It was noticeable, that the expression of *Olig2* appeared biphasic with a marked increase in levels of *Olig2* coinciding with the transition from the second to the third phase. Moreover this transition corresponded to the induction of *Ngn2*. This predicted that *Olig2* levels peak at the onset of differentiation before being downregulated as MN identity is elaborated. To test this prediction, we first examined the levels of Olig2 and Ngn2 in the neural tube of e9.5 and e10.5 embryos, during the period of MN production (Fig. 3A,B). Consistent with previous studies, we found that at both stages a proportion of Olig2 expressing cells also expressed Ngn2, while a much lower proportion of cells expressed Ngn2 outside the pMN (Mizuguchi et al. 2001; Scardigli et al. 2001; Novitch et al. 2001). To test if the levels of Olig2 expression varied in the way predicted by the single cell sequencing data, we quantified levels of Olig2, Ngn2 and the MN marker Mnx1 in nuclei of the pMN domain (Fig. 3C-F). This revealed a striking correlation between Olig2 and Ngn2 protein levels in individual cells throughout the pMN domain (Fig. 3C,E). Moreover, cells expressing high levels of Olig2 and Ngn2 were differentiating into MNs as measured by the induction of Mnx1 (Fig. 3F). This quantification also indicated that Olig2 protein persisted longer than Ngn2 in MNs, as cells co-expressing high levels of Olig2 and Mnx1, but not Ngn2, were observed (Fig. 3F). Taken together, these data suggest that high levels of Olig2 correspond to the induction of Ngn2 and the onset of neurogenesis within the pMN domain.

These data prompted us to test directly whether progenitors that expressed high levels of Olig2 were committed to MN differentiation. Since endogenous Olig2 protein disappears rapidly from differentiated MNs, we took advantage of an ESC line in which we fused the fluorescent protein mKate2 to the C-terminus of endogenous Olig2 via a self-cleaving peptide (Fig. 4A) (Shcherbo et al. 2009; Szymczak et al. 2004). In these cells, the expression of mKate2 provides a reporter of Olig2 levels but the increased stability of fluorescent protein offers a way to mark the progeny of Olig2 expressing cells and estimate the levels of Olig2 in the progenitor. Control ESC differentiations indicated that Olig2 expression dynamics, protein levels and MN formation were similar in cells containing the engineered or wild-type Olig2 allele (Fig. 4B and Figure 4-figure supplement 1A-C). Quantification of the mKate2 and Olig2 protein levels in individual nuclei revealed a positive correlation in most cells (Fig. 4C-C”,G and Figure 4-figure supplement 1D-F). However, we noticed a cohort of cells with much higher levels of mKate2 relative to Olig2. Assaying Isl1/2 expression revealed that these cells were MNs (Fig. 4D-D”). Consistent with this, high levels of Isl1/2 and Tubb3 expression were only detected in cells with high levels of mKate2 (Fig. 4H and Figure 4-figure supplement 1A-C). Moreover, mKate2 levels negatively correlated with levels of the neural progenitor marker Sox1 (Fig. 4E-E”,I). Thus, MNs indeed progress through a distinct Olig2^{HIGH} state as they exit from the NP state.

To address whether the transient upregulation of Olig2 expression was specific for the transition from pMN cells to MNs, we quantified levels of mKate2 in Nkx2.2-expressing p3 progenitors (Fig. 4F-F”). During development these progenitors transit through an Olig2-expressing pMN intermediate state before losing Olig2 expression and inducing Nkx2.2 (Chamberlain et al. 2008; Dessaud et al. 2010, 2007). In contrast to the positive correlation between Isl1/2 and mKate2 (Fig. 4H), cells expressing high levels of Nkx2.2 had low or undetectable levels of mKate2 expression (Fig. 4J and Figure 4-figure supplement 1F). Thus, distinct Olig2 expression dynamics underlie the progression of pMN cells to MN and p3 progenitors.

Inhibiting Notch signaling increases Olig2 expression

These observations raise the question of what upregulates Olig2 prior to MN formation. The Notch signalling pathway is implicated in controlling the rate of neurogenesis and inhibition of Notch signalling in NPs is well known to trigger neuronal differentiation (Artavanis-Tsakonas 1999; Selkoe and Kopan 2003;

Shimojo et al. 2011; Louvi and Artavanis-Tsakonas 2006). Furthermore, the inferred MN differentiation trajectory indicated that two canonical effectors of the Notch pathway, Hes1 and Hes5, decreased as cells switched from the early phase of Olig2^{LOW} expression to Olig2^{HIGH}. We therefore tested whether inhibiting Notch signalling upregulated Olig2. As expected, inhibition of Notch signalling, through the addition of the γ-secretase inhibitor Dibenzazepine (DBZ), for 24h between D5 and D6 of differentiation caused a substantial increase in the number of neurons observed (Fig. 4K). Quantifying mKate2 levels using flow cytometry revealed a similarly substantial increase in the number of cells expressing high levels of mKate2 (Fig. 4L and Figure 4-figure supplement 1G). Furthermore, co-staining these cells with the pan-neuronal marker Tubb3 revealed that most of the mKate2^{HIGH} cells were neurons (Figure 4-figure supplement 1I). To test whether the increase in mKate2 fluorescence is due to increased Olig2 expression upon Notch inhibition, we quantified mRNA levels of *Olig2* and other progenitor and neuronal markers using RT-qPCR after 0, 12 and 24 hours of Notch inhibition (Figure 4-figure supplement 1J-L). In contrast to other progenitor markers (*Hes1/5*, *Sox2*, *Pax6*), which decreased upon Notch inhibition (Figure 4-figure supplement 1J), *Olig2* levels peaked at 12h before decreasing after 24h, (Figure 4-figure supplement 1K). The observed *Olig2* expression dynamics are strikingly similar to those of other genes previously implicated in MN formation, including *Ngn2* and *Pou3f2* (Figure 4-figure supplement 1K). Consistent with the increase in the expression of neurogenic markers after 12h, we also observed an increase in the expression of neuronal genes 12h and 24h after Notch inhibition (Figure 4-figure supplement 1L). Taken together, these data suggest that Notch signalling controls the transition between the distinct phases of *Olig2* expression by restraining *Olig2* expression in pMN progenitors.

Olig2 represses the expression of Hes1 / Hes5

To test whether the upregulation of Olig2 coincided with the downregulation of Hes1 and Hes5 *in vivo* we examined the expression of these proteins in mouse embryos. Hes1 is broadly expressed by dorsal progenitors that express the homeodomain protein Pax3, as well as floor plate and p3 cells, marked by the expression of Foxa2 and Nkx2.2, respectively (Fig. 5B,C,F,G) (Hatakeyama et al. 2004). By contrast, Hes5 is expressed by cells in the intermediate spinal cord, marked by the expression of Irx3 and Pax6 (Fig. 5B,D,E). Olig2 expression was first detectable at e8.5, a time at which Hes5 was broadly expressed throughout the ventral neural tube (Fig. 5M). Shortly thereafter, Olig2 and Hes5 showed a high degree of co-expression, which coincided with an increase in the number of Olig2 expressing MN progenitors (Fig. 5N-R). However, coexpression of Olig2 and Hes5 appeared to be transient, as by e9.5, Hes5 was downregulated in most Olig2+ cells, and few co-expressing cells could be found by e10.5 (Fig. 5Q). During this time, Hes1 expression was low or absent in most MN progenitors (Fig. 5H-L). The progressive decrease in Hes5 expression from Olig2+ cells was mirrored by a reciprocal increase in Ngn2 expression and, subsequently, the exit of these cells from the cell cycle and the onset of MN differentiation marker expression (Fig.5 M'-Q', Novitch et al, 2001; Miziguchi et al. 2001, Lee et al. 2005). Thus, the transient coexpression of Olig2 and Hes5 *in vivo* marks the pMN state, while the clearance of Hes5 from Olig2-positive cells coincided with the onset of Ngn2 expression and MN differentiation.

We next asked whether Olig2 might be responsible for the repression of Hes1 and Hes5 using *Olig2*$^{Cre/+}$ knock-in mice (Dessaud et al 2007; Kong et al. 2015) in which Cre protein expression can be used to demarcate the pMN in both heterozygous control and homozygous *Olig2*$^{Cre/Cre}$ mutant embryos (Fig. 6A,E). In controls, the pMN was flanked dorsally and ventrally by Hes5 and Hes1 expression, respectively, with little overlap of Cre with either protein (Fig 6C-D',I). By contrast, *Olig2* mutant spinal cords displayed a marked dorsal expansion of Hes1 and ventral expansion of Hes5 into the pMN, such that their expression domains appeared to contact one another (Fig. 6G-I). This juxtaposition was associated with a substantial decrease in the number of cells expressing Ngn2 in the pMN (Fig. 6B,F,I). Thus, Olig2 is required to maintain the boundaries of Hes1 and Hes5 and allow Ngn2 to accumulate within MN progenitors (Fig. 6J).

To address whether Olig2 expression was sufficient to repress *Hes1* and *Hes5*, we used *in ovo* electroporation to deliver retroviral expression constructs driving the expression of a myc-tagged form of Olig2 into the developing spinal cord of Hamburger-Hamilton (HH) stage 11-13 chick embryos. These conditions have been previously shown to increase Ngn2 expression (Novitch et al. 2001). Whereas mammals have a single *Hes5* gene, avians contain three *Hes5* paralogs, termed *HES5-1*, *HES5-2*, and *HES5-3*, clustered at a common genomic locus (Fig. 7A). When Olig2 was misexpressed, all three chick *HES5* genes were substantially reduced, as was the chick Hes1-related gene *HAIRY1* (Figure 6-figure supplement 1A-E). Similar results were achieved with misexpression of a dominant repressor form of Olig2 containing its bHLH DNA binding domain fused to a heterologous Engrailed transcriptional repression domain (Figure 6-figure supplement 1F-J; Novitch et al., 2001). Together, these data indicate that Olig2 plays a critical role repressing the expression of *Hes* genes within MN progenitors to promote Ngn2 expression and MN differentiation (Fig. 6J).

Olig2 acts directly on a Hes5 regulatory element

The striking effects of Olig2 on *Hes1* and *Hes5* expression prompted us to ask whether Olig2 might directly regulate these genes. Examination of chromatin immunoprecipitation data from mouse neural progenitors revealed several prominent binding sites of Olig2 in the vicinity of the two loci (Fig. 7B) (Kutejova et al., 2016, http://www.ebi.ac.uk/ena/data/view/ERX628418). Furthermore, some of these binding sites are in close proximity to previously mapped binding sites for the Notch signaling cofactor RBPJ (Li et al. 2012). Bound regions included sites close to the transcription start sites of the genes and in putative distal regulatory elements (Figure 7B). Aligning genomic sequences of the *Hes5* locus from chick, mouse, and human, indicated that one of the binding sites for Olig2 and RBPJ coincided with a highly conserved ~200 base pair element, hereafter termed Hes5(e1), that is 80% identical between mouse and human, and 53% identical between chick and mouse (Figure 7A,B). This element is 7.9 kilobases (kb) 5' to the transcriptional start site for *Hes5* in mouse, 10.5 kb 5' to the transcriptional start site in human, and in the middle of the Hes5 gene cluster in chick.

Like many bHLH proteins, Olig2 binds to canonical E-box DNA response elements with the palindromic sequence CANNTG (Lee et al. 2005). This motif was found within the most conserved central region of the Hes5(e1) element (87% identity between chick and mouse over 46 bp; 98% identity between mouse and human) (Fig. 7A). To confirm that Olig2 could bind to the Hes5(e1) element, we performed *in vitro* binding experiments using a probe comprising the conserved central region. *In vitro* translated Olig2 readily bound to the Hes5(e1) E-box, as did other bHLH proteins such as E12 and Ngn2 (Fig. 7C,D). These binding activities were abolished when the conserved E-box sequence was mutated (Fig. 7C). To test if Olig2 binding activity is enhanced by the presence of E proteins, we mixed Olig2 protein with E12, but found no evidence of either an Olig2:E12:DNA complex or enhanced binding affinity to the Hes5(e1) E-box (Fig. 7C). In addition, mixing Olig2 with Id1, a potent competitor for E protein binding, did not diminish Olig2 binding although mixing E12 and Ngn2 with Id1 completely abolished both E12 and Ngn2/E12 binding activities (Fig. 7D). The binding of both Olig2 and Ngn2 to Hes5(e1) was further confirmed through chromatin immunoprecipitation experiments (Figure 7-figure supplement 1). Taken together, these data indicate that Olig2 homodimers bind directly to a highly conserved Hes5(e1) regulatory element through a single E-box site that may be targeted by other bHLH proteins.

The Hes5(e1) Element Restricts Gene Expression from the pMN

The observation that Olig2 could bind to the conserved element within the Hes5 locus prompted us to test whether this element restricted gene expression selectively from the pMN. To test this, we generated reporter constructs consisting of Hes5(e1) with or without an intact E-box, upstream of a β-globin minimal promoter driving expression of a nuclear Enhanced Green Fluorescent Protein (EGFP) gene (Hes5(e1)-βG::*nEGFP*) (Fig. 8C). We co-electroporated these constructs into the chick spinal cord together with ah::nuclear β-galactosidase (βgal) plasmid (Fig. 8A-E). CAG- driven βgal expression appeared to be uniform throughout the dorsal-ventral axis of the neural tube (Fig. 8A,D). By contrast, Hes5(e1)-βG::*nEGFP* activity was spatially restricted, with high levels of expression in the intermediate portions of the neural tube but little if any expression in both ventral and dorsal regions (Fig. 8B). Strikingly, the ventral limit of Hes5(E1)-βG::*nEGFP* expression coincided with the dorsal border of the Olig2 expression domain (Fig. 8B,F).

To determine whether the E-box within Hes5(e1) was essential for this spatially restricted expression pattern, we compared the activity of a Hes5(e1)-βG::*nEGFP* reporter construct in which the E-box had been mutated (Hes5(e1ΔE)-βG::*nEGFP*) (Fig. 8D-F). Loss of the E-box substantially reduced the overall activity of the nEGFP reporter compared to the original construct. In addition, nEGFP expression now showed abundant overlap with Olig2 in the ventral spinal cord (Fig. 8E,F). Together, these results indicate that the Hes5(e1) element integrates both positive and negative regulatory information through its E-box.

Finally, to test whether Olig2 is responsible for the restriction of Hes5(e1)-βG::nEGFP from the pMN we generated transgenic mice containing this construct that displayed activity throughout the neuraxis (Fig. 8G). In agreement with the chick electroporation data, Hes5(e1)-βG::*nEGFP* activity was spatially restricted, with high levels of expression seen only in intermediate regions of the spinal cord where high levels of Hes5 were expressed (Fig. 8H-J). The ventral extent of Hes5(e1)-βG::*nEGFP* activity coincided with the dorsal border of the pMN with little overlap between Olig2 and GFP (Fig. 8H). By contrast, in *Olig2* mutant embryos the expression of Hes5(e1)-βG::*nEGFP* extended ventrally to reach the dorsal boundary of Nkx2.2, a result that was not seen in control embryos (Fig. 8K-P). Together, these data provide evidence that Olig2 represses expression of Hes5 from pMN at least in part through direct interactions with the E-box site within Hes5(e1).

DISCUSSION

Here, we provide a detailed molecular description of somatic MN differentiation. Single cell transcriptomics defined distinct phases of differentiation and revealed the regulatory relationships that drive progression from neural progenitors to post-mitotic motor neurons. Experimental validation confirmed these predictions and demonstrated that Olig2 plays a pivotal role coordinating growth and patterning by integrating differentiation and fate determination signals.

The trajectory of neural progenitor to motor neuron differentiation

Single cell mRNA sequencing is emerging as a powerful tool to reconstruct transcriptional changes in cells during tissue development (Shin et al. 2015; Setty et al. 2016; Trapnell et al. 2014; Treutlein et al. 2016). Here, we use pseudo-temporal ordering of cells based on their expression profile to obtain a high-resolution map of the developmental trajectory of MN differentiation (Fig 2). Examination of gene expression along this timeline revealed the dynamics of signaling pathways and transcriptional networks as cells transit from proliferative progenitors to postmitotic neurons. This computationally reconstructed trajectory accurately recapitulated the known changes in gene expression associated with MN generation *in vivo*.

Examination of the timeline revealed periods of relatively stable gene expression. Punctuating these were transition phases with marked differences in gene expression profiles, which coincided with changes in the signaling status within the cells. This is consistent with the saltatory view of cell fate specification in which differentiation proceeds through a series of metastable states separated by coordinated signal-driven changes in gene expression (Moris et al. 2016). Distinct phases in MN differentiation, corresponding to known cell types, were clearly identifiable. Expression of *Irx3* marked early, uncommitted neural progenitors, normally located in the intermediate spinal cord. These progenitors transition to pMN cells in response to Shh and retinoid signaling and this was identifiable by the upregulation of *Olig2* and downregulation of *Irx3*. In addition, distinct phases in the acquisition of postmitotic MN identity could be identified with cells expressing markers such as *Lhx3*, *Isl1/2* and *Chat* correctly positioned in the pseudotemporal ordering.

The temporal ordering provided much greater resolution of the sequence of events leading to MN commitment than previously available. In particular, the transition from pMN to MN was associated with a series of distinct and transient expression changes. This included the induction of well-known pro-neurogenic factors such as *Ngn2*, *Neurod1*, *Neurod4* and *Hes6*. Increased expression of *Olig2* was also associated with this stage. Consequently, the level of *Olig2* expression could distinguish two sequential stages in pMN progenitors during their differentiation. In the earlier phase, initiated as *Irx3* is downregulated, pMN cells express low or moderate levels of *Olig2*. This is followed by the second phase in which the levels of *Olig2* substantially increases and *Ngn2* becomes expressed at high levels. *In vivo* analysis, together with the short-term lineage tracing afforded by the Olig2-mKate2 reporter, confirmed that Olig2 upregulation coincided with the commitment to differentiate into postmitotic MNs. By contrast, in the earlier phase of pMN development, the lower levels of Olig2 appeared compatible with the transition of cells to *Nkx2.2*/*Nkx2.9* expressing p3 progenitors or to *NFIB* expressing gliogenic precursors. Together, these data provide new insight into the process of MN specification, identifying a series of distinct phases in neural progenitor differentiation to fate commitment and highlighting the changes in gene expression that characterise phase transitions.

Olig2 as a coordinator of neurogenesis

Previous studies have shown that both Olig2 and Ngn2 are required for the elaboration of MN identity and that Olig2 activity induces Ngn2 expression (Novitch et al. 2001; Mizuguchi et al. 2001; Takebayashi et al. 2002; Lu et al. 2000). Consistent with these observations, progenitors in the Olig2 expression domain differentiate at a much higher rate than cells in other progenitor domains of the neural tube (Kicheva et al. 2014; Novitch et al. 2001). Our results suggest a mechanism for this enhanced rate of neuronal differentiation. The canonical Notch effectors Hes1 and Hes5 act to suppress neurogenesis by inhibiting the expression of neurogenic bHLH proteins, thus maintaining neural progenitors in an undifferentiated state (Ohtsuka et al. 1999; Shimojo et al. 2011). Olig2 activity represses *Hes1* and *Hes5* (Figs. 6 and Figure 6-figure supplement 1) thereby allowing expression of the proneural gene *Ngn2* and downstream effectors such as *Neurod4*. The ability of Olig2 to repress *Hes5* appears to be direct, as Olig2 binds to a conserved regulatory element within the *Hes5* locus that restricts gene expression from MN progenitors (Fig. 7, 8). Similarly, Olig2 binding sites are found in putative regulatory elements associated with the *Hes1* gene, raising the possibility that this regulatory interaction is also direct. Consistent with a role for Olig2 in promoting neuronal differentiation, the levels of Olig2 transcript and protein peak at the onset of neurogenesis, concomitant with the induction of Ngn2 *in vivo* and *in vitro* (Fig 2, 3). These findings therefore reveal a mechanism by which neural patterning and neurogenesis intersect. In this view, by modulating the Notch pathway, the Shh and retinoid-dependent induction of Olig2 not only specifies MN identity but also determines the rate at which these progenitors differentiate, thus imposing the distinctive kinetics of MN production.

This model is surprising as previous studies suggested antagonistic activities for Olig2 and Ngn2 during the induction of neuronal target genes (Lee et al. 2005). Both Olig2 and Ngn2 have been shown to heterodimerise with E47 and bind to E-box elements but with opposing activities (Lee et al. 2004, 2005). In addition, similar to Id proteins, Olig2 proteins could potentially sequester E proteins (E12 and E47) from forming heterodimeric Ngn2/E-protein complexes that activate transcription (Samanta and Kessler 2004; Lee et al. 2005). The sequential expression of Olig2 and Ngn2 has been proposed as a potential mechanism to reconcile the inhibitory activity of Olig2 on neurogenesis with the high rate of neurogenesis in the pMN domain (Lee et al. 2005). However, our results suggest that this mechanism is unlikely to apply to the differentiation of MNs in the spinal cord for several reasons. The higher temporal resolution provided by the pseudotemporal ordering revealed that primary Ngn2 target genes such as *Dll1* and *Neurod4* are induced when the rate of Olig2 expression is maximal in cells (Figs. 2E and Figure 2-figure supplement 1B). Furthermore, Olig2 protein perdures longer in differentiating MNs than Ngn2, resulting in significant co-expression of Olig2 and early MN markers such as Lhx3 and Mnx1 in Ngn2-negative cells (Fig. 3F and Figure 3-figure supplement 1B,C). Hence, instead of sequential expression of these proteins, these results suggest that Ngn2 is capable of mediating neurogenesis despite the presence of high levels of Olig2.

A potential solution to this puzzle may be that the activities of both Olig2 and Ngn2 are regulated by phosphorylation. Olig2 phosphorylation at specific Ser/Thr residues regulates its choice of dimerization partner, intracellular localization and DNA binding preference for open and closed chromatin (Sun et al. 2011; Meijer et al. 2014; Li et al. 2011; Setoguchi and Kondo 2004). Indeed, homodimeric complexes of Olig2 appear to mediate Hes5 repression. Similarly, phosphorylation of Ngn2 affects its stability and interaction with Lim-homeodomain TF complexes and E-proteins (Ma et al. 2008; Hindley et al. 2012; Ali et al. 2011; McDowell et al. 2014). Thus, additional post-translational events extend the regulatory interactions between both proteins beyond stochiometric interactions through protein-protein binding and competition for DNA binding sites. Notably, some of the relevant phosphorylations are performed by protein kinase A (PKA) and glycogen-synthase kinase 3 (GSK3), kinases linked to the activity of the Shh pathway, which appears to peak at the initiation of MN differentiation (Balaskas et al. 2012; Li et al. 2011; Ma et al. 2008). Connecting the activity of these neurogenic TFs to the activity of the Shh pathway would allow a tight coupling between MN generation and overall developmental dynamics dictated by the dynamics of morphogen signalling.

The pseudotemporal ordering indicated that although *Olig2* levels peaked at the onset of MN differentiation, expression then decreased rapidly, prior to MNs reaching the next metastable along the differentiation trajectory and the induction of mature MN markers such as *Isl2* and *Chat* (Fig. 2). This suggests that *Olig2* may need to be downregulated to allow progression of MN differentiation. Consistent with this, overexpression of Olig2 has been shown to inhibit the generation of MNs and to directly repress genes associated with MN identity, such as *Hb9* (Lee et al. 2004, 2005). Furthermore, the addition of Olig2 to canonical reprogramming factors decreases the efficiency of conversion from fibroblasts to spinal motor neurons (Son et al. 2011). Thus, Olig2 upregulation can promote MN generation by initiating differentiation but its downregulation is needed to complete the switch from progenitor to post-mitotic neuron. These dynamics of Olig2 expression may help ensure that the correct temporal sequence of gene expression occurs as MNs mature.

Oscillation of bHLH TFs in the spinal cord

The maintenance of neural progenitors in the brain has been ascribed to the oscillatory expression of Hes and proneural bHLH TFs (Imayoshi et al. 2013; Shimojo et al. 2008). The Hes proteins are proposed to generate the oscillations by negatively regulating their own expression as well as Ngn2 and Ascl1 (Takebayashi et al. 1994; Imayoshi and Kageyama 2014; Shimojo et al. 2011). This phenomenon results in Hes1 and proneural bHLH TFs exhibiting reciprocal expression phases at an equivalent frequency (Shimojo et al. 2008; Imayoshi et al. 2013). Oscillations in the levels of the Notch ligand Dll1 have been reported in spinal cord progenitors (Shimojo et al. 2016). In cortical progenitors, fluctuations in Olig2 levels have also been documented, but these oscillations occur at a significantly slower frequency (Imayoshi et al. 2013) and may therefore be regulated by a different mechanism.

Although we did not specifically investigate the occurrence of bHLH oscillations in the spinal cord *in vitro* or *in vivo*, our results may shed light on this question. The Hes5(e1) element can be bound by both Olig2-Olig2 repression and Ngn2-E12 activation complexes (Fig. 7B,C). It is notable that mutation of the E-box in this element reduced the overall level of reporter activity in the spinal cord, at the same time as disrupting its spatial restriction from the pMN (Fig. 8A). These data are consistent with a model in which positive activators, such as Ngn2 or other E-box binding factors, could interact with Hes5(e1) to directly elevate Hes5 expression, which would in turn serve to repress Ngn2 expression, thereby contributing to alternating phases of Hes5 and Ngn2 expression. In this regard, Olig2 binding and repressing Hes5 through this element would interrupt the oscillator, allowing Ngn2 expression to reach its maximal levels and neuronal differentiation to commence.

To examine Olig2 expression, we used the relatively long half-life fluorescent protein mKate2 inserted into the Olig2 genomic locus. Quantification of the levels of mKate2 and Olig2 revealed a striking correlation between both proteins in NPs (Figure 4-figure supplement 1D-F). This argues against Olig2 oscillations in these cells, as oscillatory behaviour would be expected to decrease the correlation between both proteins. Although further investigation is necessary, the data are consistent with out-of-phase oscillations between Ngn2 and Hes5, while Olig2 levels steadily increase in MN progenitors over time. Understanding these relationships will provide insight into the transition from MN progenitor to differentiation.

The Notch pathway regulates Olig2 expression and Shh signaling

Besides promoting neurogenesis, inhibition of Notch effectors also appears to be important for dorsal-ventral patterning of the neural tube and the consolidation of pMN identity. Patterning of the ventral neural tube is mediated by a gene regulatory network that interprets both levels and duration of Shh signalling (Balaskas et al. 2012; Cohen et al. 2014; Dessaud et al. 2010). Previous studies have suggested that Notch signalling influences patterning of the ventral spinal cord by promoting the activity of the Shh pathway (Kong et al. 2015; Stasiulewicz et al. 2015). Consistent with this, overexpression of cHairy2, the chick homologue of murine Hes1, causes a downregulation of Olig2 and induction of Nkx2.2 in the pMN domain (Stasiulewicz et al. 2015). Similarly, sustained activation or inhibition of the Notch pathway causes, respectively, a ventral expansion or recession in p3 progenitors, located ventral to the pMN (Kong et al. 2015). Here, we show that besides modulating Shh activity, Notch signalling can also regulate expression levels of Olig2. Conversely, Olig2 represses the canonical Notch effector Hes5 and could thereby negatively regulate the levels of Shh signalling in the pMN domain. Thus, Olig2 may consolidate pMN identity not only by direct repression of other progenitor markers, but also indirectly by modulating levels of Shh signalling through its effect on Notch pathway.

Taken together, our data reveal a tight coupling between the gene regulatory networks that control patterning and differentiation in the ventral spinal cord. They highlight the pivotal role of Olig2 in this process, which not only acts as central organizer of DV patterning in the spinal cord, but also as developmental pacemaker for MN formation. The Olig2-mediated repression of Notch pathway targets provides a molecular mechanism for the much higher rate of neurogenesis observed in the pMN domain compared to the rest of the spinal cord and thereby explains the spatial and temporal patterns of neurogenesis observed in the neural tube. These findings raise the question of whether similar mechanisms also apply in other progenitor domains in the neural tube.

EXPERIMENTAL PROCEDURES

Animal Welfare

Animal experiments in the Briscoe lab were performed under UK Home Office project licenses (PPL80/2528 and PD415DD17) within the conditions of the Animal (Scientific Procedures) Act 1986. Animals were only handled by personal license holders. *Olig2*^{Cre} knock-in/knockout mice were used as previously described (Dessaud et al., 2007), and interbred to create Olig2 mutant embryos. All mice in the Novitch lab were maintained and tissue collected in accordance with guidelines set forth by the UCLA Institutional Animal Care and Use Committee. Fertilized chicken eggs were acquired from AA McIntyre Poultry and Fertile Eggs, incubated and electroporated as previously described (Gaber et al. 2013).

Differentiation of NPs from mouse ESCs

NPs were differentiated as described previously (Gouti et al. 2014). In brief, HM1 (Thermo Scientific), DVI2 and Olig2::T2A-mkate2 ESCs were maintained in ES cell medium with 1000 U/ml LIF on mitotically inactivated mouse embryonic fibroblasts (feeder cells). DVI2 cells were generated by integrating a 8xGBS-H2B::Venus Shh pathway reporter into the HPRT locus of HM1 cells and used for all ESC experiments except 4-color stainings in Figure 3-figure supplement 1A,B, which rely on HM1 cells, and experiments in Figs. 4 and Figure 4-figure supplement 1 which were conducted using the Olig2::T2A-mKate2 reporter cell line.

For differentiation cells were dissociated in 0.05% Trypsin (Gibco) and replated onto tissue culture plates for 25 minutes to remove feeder cells. Cells staying in the supernatant were spun down and resuspended in N2B27 medium at a concentration of 10^6 cells / ml. 45000 cells were plated onto 35 mm CellBind dishes (Corning) precoated with 0.1% Gelatine solution in 1.5 ml N2B27 + 10 ng / ml bFGF. At D2 medium was replaced with N2B27 + 10 ng / ml bFGF + 5 μM CHIR99021 (Axon). At D3, and every 24 hours afterwards, medium was replaced with N2B27 + 100 nM RA (Sigma) + 500 nM SAG (Calbiochem). For Notch inhibition differentiations were treated at D5 with N2B27 + 100 nM RA + 500 nM SAG + 10 ng/μl DBZ (Tocris Biosciences) for 24 hours. Cells were washed with N2B27 medium at later medium changes when many dead cells were detected in the dish.

qPCR analysis

mRNA was extracted using RNeasy Mini Kit (Qiagen) according to the manufacturer's instructions. 2μg of RNA was used for reverse transcription using Super-Script III First-Strand Synthesis kit (Invitrogen) with random hexamers. Platinum SYBR Green qPCR mix (Invitrogen) was used for amplification on a 7900HT Fast Real Time PCR machine (Applied Biosystems). Expression values were normalized against β-actin. Three independent repeats of each qPCR time-course were performed and three independent samples at each time point of each repeat were analyzed. For a complete list of used primers see Table S1. qPCR data presented in Fig. 1, Figure 1-figure supplement 1 and Figure 4-figure supplement 1 shows one representative repeat and shows mean +/- standard deviation.

Immunofluorescent stainings

Cells were washed using N2B27 medium and PBS (Gibco) and then fixed in 4% paraformaldehyde in PBS at 4°C for 20 minutes. After fixation cells were washed twice with PBS and stored in a fridge till stainings were perfomed. For staining, cells were washed three times in PBS containing 0.1% Triton X-100 (PBS-T). Primary and secondary antibodies were diluted in PBS-T + 1% BSA. Cells were incubated with primary antibodies overnight at 4°C, then washed three times for 5-10 minutes in PBS-T, incubated with secondary antibodies for 1 hour at room temperature, and washed again three times in PBS-T. Stainings were mounted using ProLong Gold Antifade reagent (Life Technologies). Mouse and chicken spinal cord tissues were fixed with 4% paraformaldehyde, cryoprotected in 30% sucrose, sectioned, and processed for immunohistochemistry or in situ hybridization as previously described (Sasai et al. 2014; Gaber et al. 2013).

Antibodies against a peptide in the C-terminal portion of mouse Hes5 (APAKEPPAPGAAPQPARSSAK, aa 127-147) were raised in rabbits and guinea pigs (Covance). The rabbit serum was affinity purified and used at 1:8000, and the crude guinea pig serum at 1:16000. Additional primary antibodies were used as follows: goat anti-β-galactosidase (Biogenesis 4600-1409 1:2000), mouse anti-Cre (Covance Covance MMS-106P, 1:2000), rat anti-FLAG (Stratagene 200474, 1:1500), sheep anti-GFP (AbD Serotec 4745-1051, 1:800), rabbit anti-Hes1 (Ito et al. 2000, 1:1000), mouse anti-Hoxc6 (Santa Cruz Biotechnology sc-376330, 1:250), mouse anti-Hb9 (DSHB, 1:40), mouse anti-Islet1/2 (DSHB, 1:100), goat anti-Islet1 (R&D AF1837, 1:1000), rabbit anti-Lhx3 (Abcam ab14555, 1:500), goat anti-Ngn2 (Santa Cruz Biotechnology sc-19233, 1:500), mouse anti-Ngn2 (5C6, Lo et al. 2002, 1:50), mouse anti-Nkx2.2 (DSHB, 1:25), guinea pig anti-Olig2 (Novitch et al. 2001, 1:20000), rabbit anti-Olig2 (Millipore AB9610, 1:1000), rabbit anti-Pax6 (Millipore AB2237, 1:1000), mouse anti-Pax6 (DSHB, 1:25), goat anti-Sox1 (R&D AF3369, 1:500), rabbit anti-TagRFP (Evrogen AB233, 1:1000), rabbit anti-Tubb3 (Covance PRB-435P, 1:2000), mouse anti-Tubb3 (Covance MMS-435P, 1:1000), rabbit anti-Zbtb18 (Proteintech 12714-1-AP, 1:1000).

Secondary antibodies used throughout this study were raised in donkey. Alexa488, Alexa568, Cy3, and Dylight 647-conjugated antibodies (Life Technologies or Jackson Immunoresearch) were diluted 1:1000, Alexa647 conjugated antibodies (Life Technologies) 1:500. Cy5 conjugated antibodies (Jackson Immunoresearch) 1:700, CF405M donkey anti-guinea pig secondary antibody (Sigma) 1:250.

Image acquisition and analysis

Immunofluorescent images of ESC-derived NPs were acquired using a Zeiss Imager.Z2 microscope equipped with an Apotome.2 structured illumination module and a 20x magnification lens (NA = 0.75). 5 phase images were acquired for structured illumination. For each image z-stacks comprised of 12 sections separated by 1 μm were acquired. Maximum intensity projection was performed in Fiji.

Cryosections were documented using a Leica SP5 confocal microscope equipped with a 40x oil objective, or Zeiss LSM5, LSM700, or LSM800 confocal microscopes and Zeiss Apotome imaging systems equipped with 10x, 20x, and 40x oil objectives. For nuclear staining intensity measurements 3-4 individual sections separated by 1 μm were analysed. Nuclei segmentation and intensity measurement were performed in CellProfiler. Data was normalized and plotted using R. Other images were processed and manually quantified using Fiji and Adobe Photoshop imaging software.

Single Cell Sequencing

NPs were dissociated using 0.05% Trypsin (Gibco), spun down in ES-medium, resuspended, washed and spun down in 10 ml PBS (Gibco). Afterwards, cells were resuspended in 1ml N2B27 and filtered into a FACS tube (Falcon). The Fluidigm C1 platform was used to capture individual cells using 96 small or medium IFC chip. Cells were diluted in the range of 250 000-400 000 cells per ml for chip loading. Capturing efficiency was evaluated by manually inspecting each capture site on the chip using the automated NanoEntek JuLi cell imager. Only capture sites containing single cells were processed for library preparation and sequencing. Single cell cDNA was generated using the Clontech SMARTer Ultra Low RNA kit on the C1 chip using manufacturer-provided protocol. ArrayControl RNA Spikes (AM1780) were added to the cell lysis mix as recommended in the Fluidigm protocol. Libraries were prepared using the Illumina Nextera XT DNA Sample Preparation kit according to a protocol supplied by Fluidigm, and sequenced on Illumina Hiseq 4000 for 75bp paired-end runs.

Generation of Olig2::T2A-mKate2 ESC line by CRISPR

pNTKV-T2A-3xNLS-FLAG-mKate2 was generated by cloning a T2A-3XNLS-FLAG-mKate2 cassette into pNTKV using HpaI and HindIII restriction sites. To integrate the T2A-3xNLS-FLAG-mKate2 cassette at the 3' end of the Olig2 open reading frame, a donor vector comprising app. 2.8 kb upstream and 5 kb downstream of the Stop-Codon was constructed. For CRISPR/Cas9 mediated homologous recombination, a short guide RNA (sgRNA) sequence (CGGCCAGCGGGGGTGCGTCC) was cloned into pX459 (Addgene) according to (Ran et al. 2013).

For electroporation DVI2 ESCs were grown in 2i medium + LIF. 4μg of both plasmids were electroporated into $4*10^6$ cells using Nucleofector II (Amaxa) and mouse ESC Nucleofector kit (Lonza). Afterwards, cells were replated onto 10 cm CellBind plates (Corning) and maintained in 2i medium + LIF. For selection cells were first treated with 1.5 μg/ml Puromycin (Sigma) for two days and afterwards with 50 μg/ml Geniticin (Gibco) until colonies were clearly visible. Individual colonies were picked using a 2 μl pipette, dissociated in 0.25% Trypsin (Gibco) and replated onto feeder cells in ES-medium + 1000 U/ml LIF in a 96 well plate. Correct integration of the T2A-3xNLS-FLAG-mKate2 transgene was verified using long-range PCRs.

Western Blots

Cells were lysed in RIPA buffer supplemented with protease inhibitors. 10 μg of total protein was loaded per lane. Antibodies used were rabbit anti-Olig2 (Millipore AB9610, 1:3000) and mouse anti-β-tubulin (Sigma T4026, 1:2000). Secondary antibodies were donkey anti-mouse IRDye 800CW and donkey anti-rabbit IRDye 680RD (both Licor). Blots were scanned using an Odyssey Scanner (Licor).

Flow Cytometry

To quantify the number of Olig2::T2A-mKate2 positive cells, NPs were trypsinized in 0.05% Trypsin (Gibco) and spun down in ES medium. Cells were resuspended in PBS (Gibco) supplemented with the live-cell staining dye Calcein Violet (Life Technologies) according to the manufacturer's instructions. Flow analysis was performed using a Becton Dickinson LSRII flow cytometer. HM1 or DVI2 cells were differentiated in parallel and analyzed using the same settings to estimate the number of mKate2 fluorescent cells. The threshold for counting cells as mKate2 positive was set to 0.5% of positive cells in cells without mKate2 fluorescence. 30000 events were recorded for each replicate.

For analysis of Tubb3 stainings by flow cytometry, cells were fixed for 20 minutes in 2% PFA on ice, washed three times in PBS-T and incubated with Alexa647-conjugated anti-Tubb3 antibody (BD Pharmingen, 1:10) in PBS-T + 1% BSA for one hour at room temperature. Cells were afterwards washed 3x in PBS-T and endogenous mKate2 fluorescence and Tubb3 staining in 10000 cells were quantified by flow cytometry. Data was analyzed using FlowJo.

Electrophoretic Mobilty Shift assays

pCS2+ plasmid expression vectors for Olig2, E12, Ngn2, and Id1 (Novitch et al. 2001) were transcribed and translated *in vitro* using the Promega TNT Coupled Wheat Germ Extract System. Programmed extracts were mixed as indicated in a buffer containing 100 mM Hepes pH 7.6, 25 mM KCl, 1.5 mM MgCl2, 0.2 mM EDTA, 2.5% glycerol, and 100 ng poly dIdC and incubated for 15 min at room temperature. ^{32}P-dCTP-labeled probes were generated by Klenow end-labeling of double stranded oligonucleotides containing the native mouse Hes5(e1) sequence (forward 5’-ggccgCTCCCAAAAGACCATCTGGCTCCGTGTTATAA-3’; reverse 5’-actagTTATAACACGGAGCCAGATGGTCTTTTGGGAG-3’) or an E-box mutated version (forward 5’ ggccgCTCCCAAAAGAggATCccGCTCCGTGTTATAA-3’; reverse 5’-actagTTATAACACGGAGCggGATccTCTTTTGGGAG-3’). The E-box sequence is underlined. Lower case indicates substitutions and added flanking sequences. Samples were incubated with labeled probes for 15 min before resolving on a 4.5% polyacrylamide gel and subsequent autoradiography. Probe competition was achieved by incorporating unlabeled oligonucleotide probes in the binding reaction mix.

Hes5(e1) Transgenic Assays

Mouse and chick Hes5(e1) genomic DNA fragments were amplified by PCR and cloned into a reporter construct containing the β-globin basal promoter, a nuclear EGFP coding sequence, and a bovine growth hormone polyadenylation sequence (βG::nGFP, Lumpkin et al. 2003). Mutations of the Hes5(e1) E-box were generated through splicing by overlap extension PCR. Chick embyos were co-electroporated with chick Hes5(e1) constructs along with a plasmid vector producing nuclear-tagged β-galactosidase under the control of the cytomegalovirus enhancer and β-actin promoter. Embryos were collected, fixed, and cryosectioned. Sections were stained using antibodies to β-galactosidase and Olig2 and fluorescent secondary antibodies. GFP levels were measured based on its native fluorescence. Images were collected and positions of cells expressing each marker rendered using the spots function of the Bitplane Imaris 8.4 imaging suite. Calculated positions were exported and processed using Microsoft Excel and Graphpad Prism 7 software.

Transgenic mice expressing the mouse Hes5(e1)-βG::nGFP reporter were generated with the assistance of the University of Michigan Transgenic Animal Model Core by microinjection of purified plasmid DNA into fertilized eggs obtained by mating (C57BL/6 X SJL)F1 female mice with (C57BL/6 X SJL)F1 male mice, and subsequent transfer to pseudopregnant recipients. Analysis was conducted on both embryos collected from the primary reporter injections and offspring collected from matings of a transgenic line that passed through the germline.

Electroporation and In situ hybridization

Chick embryos were electroporated at Hamburger-Hamilton (HH) stages 11-13 with RCAS-myc-tagged chick Olig2 and Olig2-bHLH-Engrailed plasmid constructs (Novitch et al., 2001) and collected at HH stages 21-23. Spinal cord sections were hybridized with digoxigenin-UTP labeled RNA probes generated from plasmid DNA or templates generated by PCR. 3' UTR sequences for chick *HES5-1* and *HES5-3* were amplified from spinal cord cDNA with the following primers: *HES5-1*, forward 5'-GCGGAATTCAGGGAAGCTCTCACTTAGTGAAC-3' and reverse 5'-GCGCTCGAGATACCCTCCTGCTGAAGACATTTGC-3'; *HES5-3*, forward 5'-GCGGAATTCGCCAAGAGCACGCTCACCATCACCT-3' and reverse 5'-GCGCTCGAGCTACACAGCTTGAGTTATGGTTTAG-3' and directionally cloned into the pBluescript. Underlined sequence indicates restriction enzyme sites incorporated into the primers. Chick *HAIRY1* and *HES5-2* 3' UTR riboprobes were generated as previously described (Gaber et al. 2013).

Chromatin Immunopreciptation-PCR

ES cell-derived motor neuron progenitors were dounce homogenized and sonicated in 3 ml lysis buffer (1% SDS, 50 mM Tris pH 8.0, 20 mM EDTA, 1 mM PMSF, and 1X Complete protease inhibitor cocktail (Roche). 150 μg of lysate DNA were used per immunoprecipitation reaction and mixed with 3-5 μl of either rabbit anti-Olig2 antibodies (Millipore AB9610), rabbit anti-Ngn2 serum (generous gift of Dr. Soo-Kyung Lee, Oregon Health Sciences University), normal rabbit sera, or purified rabbit IgG. Antibody-chromatin complexes were collected using Dynabeads protein A (Invitrogen), washed and eluted DNA used for RT-qPCR in triplicate using the following primer pairs: *Hes5(e1)* forward 5'-CTGCTTCTGAATGAATGAGGGCGG-3' and reverse 5'-AGCAGACGAGCCCTTTATTGCTCT-3'; *Hes5(e2)*, a non-conserved element 3' to the Hes5 coding exons that contains an E box, forward 5'-AGATGGCTCAGCGGTTAAGAG-3' and reverse 5'-CCATGTGGTTGCTGGGATTTG-3'. Fold enrichment for each region was calculated as compared to normal rabbit serum or purified IgG.

AUTHOR CONTRIBUTIONS

AS, ZG, JD, Conception and Design, Acquisition of Data, Analysis and interpretation of data, Drafting or revising the article, Contributed unpublished, essential data or reagents; JK, DR, CP, SW, NMG, Acquisition of Data, Analysis and interpretation of data, Contributed unpublished, essential data or reagents; JB, Conception and Design, Analysis and interpretation of data, Drafting or revising the article; BN, Conception and Design, Acquisition of Data, Analysis and interpretation of data, Drafting or revising the article

ACKNOWLEDGEMENTS

We are grateful to Leena Bhaw and Abdul Sesay for excellent support with single cell sequencing, Supraja Varadarajan for assistance with Imaris image processing and Vicki Metzis for help with processing and visualizing ChIP-Seq data. We thank David Anderson, Thomas Jessell, Soo-Kyung Lee, Susan Morton, and Tetsuo Sudo for reagents; Lorena Belen Garcia Perez, Teresa Rayon Alonso and Christopher Demers for comments on the manuscript. The Hes5 antisera were generated in Thomas Jessell's laboratory with support from the Howard Hughes Medical Institute and NINDS. AS has received funding from an EMBO LTF (1438-2013), HFSP LTF (LT000401/2014-L) and the People Programme (Marie Curie Actions) of the European Union's Seventh Framework Programme FP7-2013 under REA grant agreement n° 624973. Work in JB's lab was supported by the Francis Crick Institute which receives its funding from Cancer Research UK (FC001051), the UK Medical Research Council (FC001051), and the Wellcome Trust (FC001051; WT098326MA). Work in BN's lab was supported by the UCLA Broad Stem Cell Research Center, the NINDS (R01NS053976, R01NS072804, and R01NS085227, the March of Dimes Foundation (5-FY06-7), and the Whitehall Foundation (2004-05-90-APL).

REFERENCES

Alaynick WA, Jessell TM, Pfaff SL. 2011. SnapShot: Spinal cord development. *Cell* **146**: 178.e1.

Ali F, Hindley C, McDowell G, Deibler R, Jones A, Kirschner M, Guillemot F, Philpott A. 2011. Cell cycle-regulated multi-site phosphorylation of Neurogenin 2 coordinates cell cycling with differentiation during neurogenesis. *Development* **138**: 4267–4277.

Arber S, Han B, Mendelsohn M, Smith M, Jessell TM, Sockanathan S. 1999. Requirement for the homeobox gene Hb9 in the consolidation of motor neuron identity. *Neuron* **23**: 659–674.

Artavanis-Tsakonas S. 1999. Notch Signaling: Cell Fate Control and Signal Integration in Development. *Science (80-)* **284**: 770–776.

Balaskas N, Ribeiro A, Panovska J, Dessaud E, Sasai N, Page KM, Briscoe J, Ribes V. 2012. Gene regulatory logic for reading the Sonic Hedgehog signaling gradient in the vertebrate neural tube. *Cell* **148**: 273–284.

Bertrand N, Castro DS, Guillemot F. 2002. Proneural genes and the specification of neural cell types. *Nat Rev Neurosci* **3**: 517–530.

Briscoe J, Ericson J. 1999. The specification of neuronal identity by graded Sonic Hedgehog signalling. *Semin Cell Dev Biol* **10**: 353–362.

Briscoe J, Pierani A, Jessell TM, Ericson J. 2000. A homeodomain protein code specifies progenitor cell identity and neuronal fate in the ventral neural tube. *Cell* **101**: 435–445.

Brunskill EW, Witte DP, Shreiner AB, Potter SS. 1999. Characterization of Npas3, a novel basic helix-loop-helix PAS gene expressed in the developing mouse nervous system. *Mech Dev* **88**: 237–241.

Cahoy JD, Emery B, Kaushal A, Foo LC, Zamanian JL, Christopherson KS, Xing Y, Lubischer JL, Krieg PA, Krupenko SA, et al. 2008. A Transcriptome Database for Astrocytes, Neurons, and Oligodendrocytes: A New Resource for Understanding Brain Development and Function. *J Neurosci* **28**: 264–278.

Chamberlain CE, Jeong J, Guo C, Allen BL, McMahon AP. 2008. Notochord-derived Shh concentrates in close association with the apically positioned basal body in neural target cells and forms a dynamic gradient during neural patterning. *Development* **135**: 1097–1106.

Chen JA, Huang YP, Mazzoni EO, Tan GC, Zavadil J, Wichterle H. 2011. Mir-17-3p controls spinal neural progenitor patterning by regulating Olig2/Irx3 cross-repressive loop. *Neuron* **69**: 721–735.

Cohen M, Briscoe J, Blassberg R. 2013. Morphogen interpretation: the transcriptional logic of neural tube patterning. *Curr Opin Genet Dev* **23**: 423–428.

Cohen M, Page KM, Perez-Carrasco R, Barnes CP, Briscoe J. 2014. A theoretical framework for the regulation of Shh morphogen-controlled gene expression. *Development* **141**: 3868–3878.

Dasen JS, Liu J-P, Jessell TM. 2003. Motor neuron columnar fate imposed by sequential phases of Hox-c activity. *Nature* **425**: 926–933.

Davidson EH. 2010. Emerging properties of animal gene regulatory networks. *Nature* **468**: 911–920.

Dessaud E, Ribes V, Balaskas N, Yang LL, Pierani A, Kicheva A, Novitch BG, Briscoe J, Sasai N. 2010. Dynamic assignment and maintenance of positional identity in the ventral neural tube by the morphogen sonic hedgehog. *PLoS Biol* **8**: e1000382.

Dessaud E, Yang LL, Hill K, Cox B, Ulloa F, Ribeiro A, Mynett A, Novitch BG, Briscoe J. 2007. Interpretation of the sonic hedgehog morphogen gradient by a temporal adaptation mechanism. *Nature* **450**: 717–720.

Ericson J, Thor S, Edlund T, Jessell TM, Yamada T. 1992. Early stages of motor neuron differentiation revealed by expression of homeobox gene Islet-1. *Science (80-)* **256**: 1555 LP-1560.

Gaber ZB, Butler SJ, Novitch BG. 2013. PLZF regulates fibroblast growth factor responsiveness and maintenance of neural progenitors. ed. F. Polleux. *PLoS Biol* **11**: e1001676.

Gouti M, Tsakiridis A, Wymeersch FJ, Huang Y, Kleinjung J, Wilson V, Briscoe J. 2014. In vitro generation of neuromesodermal progenitors reveals distinct roles for wnt signalling in the specification of spinal cord and paraxial mesoderm identity. *PLoS Biol* **12**: e1001937.

Hatakeyama J, Bessho Y, Katoh K, Ookawara S, Fujioka M, Guillemot F, Kageyama R. 2004. Hes genes regulate size, shape and histogenesis of the nervous system by control of the timing of neural stem cell differentiation. *Development* **131**: 5539–5550.

Hindley C, Ali F, McDowell G, Cheng K, Jones A, Guillemot F, Philpott A. 2012. Post-translational modification of Ngn2 differentially affects transcription of distinct targets to regulate the balance between progenitor maintenance and differentiation. *Development* **139**: 1718–1723.

Imayoshi I, Isomura A, Harima Y, Kawaguchi K, Kori H, Miyachi H, Fujiwara T, Ishidate F, Kageyama R. 2013. Oscillatory control of factors determining multipotency and fate in mouse neural progenitors. *Science (80-)* **342**: 1203–1208.

Imayoshi I, Kageyama R. 2014. bHLH factors in self-renewal, multipotency, and fate choice of neural progenitor cells. *Neuron* **82**: 9–23.

Ito T, Udaka N, Yazawa T, Okudela K, Hayashi H, Sudo T, Guillemot F, Kageyama R, Kitamura H. 2000. Basic helix-loop-helix transcription factors regulate the neuroendocrine differentiation of fetal mouse pulmonary epithelium. *Development* **127**: 3913–21.

Jeong J, McMahon AP. 2005. Growth and pattern of the mammalian neural tube are governed by partially overlapping feedback activities of the hedgehog antagonists patched 1 and Hhip1. *Development* **132**: 143–154.

Jessell TM. 2000. Neuronal specification in the spinal cord: inductive signals and transcriptional codes. *Nat Rev Genet* **1**: 20–29.

Kageyama R, Ohtsuka T, Kobayashi T. 2007. The Hes gene family: repressors and oscillators that orchestrate embryogenesis. *Development* **134**: 1243–1251.

Kicheva A, Bollenbach T, Ribeiro A, Valle HP, Lovell-Badge R, Episkopou V, Briscoe J. 2014. Coordination of progenitor specification and growth in mouse and chick spinal cord. *Science* **345**: 1254927.

Kong JH, Yang L, Briscoe J, Novitch BG, Kong JH, Yang L, Dessaud E, Chuang K, Moore DM, Rohatgi R. 2015. Notch Activity Modulates the Responsiveness of Neural Progenitors to Sonic Hedgehog Signaling. *Dev Cell* **33**: 373–387.

Kutejova E, Sasai N, Shah A, Gouti M, Briscoe J. 2016. Neural Progenitors Adopt Specific Identities by Directly Repressing All Alternative Progenitor Transcriptional Programs. *Dev Cell* **36**: 639–653.

Lacomme M, Liaubet L, Pituello F, Bel-Vialar S. 2012. NEUROG2 Drives Cell Cycle Exit of Neuronal Precursors by Specifically Repressing a Subset of Cyclins Acting at the G1 and S Phases of the Cell Cycle. *Mol Cell Biol* **32**: 2596–2607.

Lee SK, Jurata LW, Funahashi J, Ruiz EC, Pfaff SL. 2004. Analysis of embryonic motoneuron gene regulation: derepression of general activators function in concert with enhancer factors. *Development* **131**: 3295–3306.

Lee SK, Lee B, Ruiz EC, Pfaff SL. 2005. Olig2 and Ngn2 function in opposition to modulate gene expression in motor neuron progenitor cells. *Genes Dev* **19**: 282–294.

Lee SK, Pfaff SL. 2001. Transcriptional networks regulating neuronal identity in the developing spinal cord. *Nat Neurosci* **4 Suppl**: 1183–1191.

Li H, de Faria JP, Andrew P, Nitarska J, Richardson WD. 2011. Phosphorylation regulates OLIG2 cofactor choice and the motor neuron-oligodendrocyte fate switch. *Neuron* **69**: 918–929.

Li Y, Hibbs MA, Gard AL, Shylo NA, Yun K. 2012. Genome-Wide Analysis of N1ICD/RBPJ Targets In Vivo Reveals Direct Transcriptional Regulation of Wnt, SHH, and Hippo Pathway Effectors by Notch1. *Stem Cells* **30**: 741–752.

Lo L, Dormand E, Greenwood A, Anderson DJ. 2002. Comparison of the generic neuronal differentiation and neuron subtype specification functions of mammalian achaete-scute and atonal homologs in cultured neural progenitor cells. *Development* **129**: 1553–1567.

Louvi A, Artavanis-Tsakonas S. 2006. Notch signalling in vertebrate neural development. *Nat Rev Neurosci* **7**: 93–102.

Lu QR, Sun T, Zhu Z, Ma N, Garcia M, Stiles CD, Rowitch DH. 2002. Common Developmental Requirement for Olig Function Indicates a Motor Neuron/Oligodendrocyte Connection. *Cell* **109**: 75–86.

Lu QR, Yuk D, Alberta J a, Zhu Z, Pawlitzky I, Chan J, McMahon AP, Stiles CD, Rowitch DH. 2000. Sonic Hedgehog–Regulated Oligodendrocyte Lineage Genes Encoding bHLH Proteins in the Mammalian Central Nervous System. *Neuron* **25**: 317–329.

Ma YC, Song MR, Park JP, Henry Ho HY, Hu L, Kurtev M V., Zieg J, Ma Q, Pfaff SL, Greenberg ME. 2008. Regulation of Motor Neuron Specification by Phosphorylation of Neurogenin 2. *Neuron* **58**: 65–77.

McDowell GS, Hindley CJ, Lippens G, Landrieu I, Philpott A. 2014. Phosphorylation in intrinsically disordered regions regulates the activity of Neurogenin2. *BMC Biochem* **15**: 24.

Meijer DH, Sun Y, Liu T, Kane MF, Alberta JA, Adelmant G, Kupp R, Marto JA, Rowitch DH, Nakatani Y, et al. 2014. An Amino Terminal Phosphorylation Motif Regulates Intranuclear Compartmentalization of Olig2 in Neural Progenitor Cells. *J Neurosci* **34**: 8507–8518.

Mizuguchi R, Sugimori M, Takebayashi H, Kosako H, Nagao M, Yoshida S, Nabeshima YI, Shimamura K, Nakafuku M. 2001. Combinatorial roles of Olig2 and Neurogenin2 in the coordinated induction of pan-neuronal and subtype-specific properties of motoneurons. *Neuron* **31**: 757–771.

Moris N, Pina C, Arias AM. 2016. Transition states and cell fate decisions in epigenetic landscapes. *Nat Rev Genet* **17**: 693–703.

Novitch BG, Chen AI, Jessell TM. 2001. Coordinate regulation of motor neuron subtype identity and pan-neuronal properties by the bHLH repressor Olig2. *Neuron* **31**: 773–789.

Ohtsuka T, Ishibashi M, Gradwohl G, Nakanishi S, Guillemot F, Kageyama R. 1999. Hes1 and Hes5 as notch effectors in mammalian neuronal differentiation. *EMBO J* **18**: 2196–2207.

Oosterveen T, Kurdija S, Ensterö M, Uhde CW, Bergsland M, Sandberg M, Sandberg R, Muhr J, Ericson J. 2013. SoxB1-driven transcriptional network underlies neural-specific interpretation of morphogen signals. *Proc Natl Acad Sci U S A* **110**: 7330–5.

Philippidou P, Dasen JS. 2013. Hox Genes: Choreographers in Neural Development, Architects of Circuit Organization. *Neuron* **80**: 12–34.

Ran FA, Hsu PD, Lin CY, Gootenberg JS, Konermann S, Trevino AE, Scott DA, Inoue A, Matoba S, Zhang Y, et al. 2013. Double nicking by RNA-guided CRISPR Cas9 for enhanced genome editing specificity. *Cell* **154**: 1380–1389.

Rhee HS, Closser M, Guo Y, Bashkirova E V., Tan GC, Gifford DK, Wichterle H. 2016. Expression of Terminal Effector Genes in Mammalian Neurons Is Maintained by a Dynamic Relay of Transient Enhancers. *Neuron* 1–14.

Ribes V, Briscoe J. 2009. Establishing and interpreting graded Sonic Hedgehog signaling during vertebrate neural tube patterning: the role of negative feedback. *Cold Spring Harb Perspect Biol* **1**: a002014.

Samanta J, Kessler JJA. 2004. Interactions between ID and OLIG proteins mediate the inhibitory effects of BMP4 on oligodendroglial differentiation. *Development* **131**: 4131–4142.

Sasai N, Kutejova E, Briscoe J. 2014. Integration of signals along orthogonal axes of the vertebrate neural tube controls progenitor competence and increases cell diversity. *PLoS Biol* **12**: e1001907.

Scardigli R, Schuurmans C, Gradwohl G, Guillemot F. 2001. Crossregulation between Neurogenin2 and pathways specifying neuronal identity in the spinal cord. *Neuron* **31**: 203–217.

Scialdone A, Tanaka Y, Jawaid W, Moignard V, Wilson NK, Macaulay IC, Marioni JC, Göttgens B. 2016. Resolving early mesoderm diversification through single-cell expression profiling. *Nature* 1–22.

Selkoe D, Kopan R. 2003. Notch and Presenilin: regulated intramembrane proteolysis links development and degeneration. *Annu Rev Neurosci* **26**: 565–97.

Setoguchi T, Kondo T. 2004. Nuclear export of OLIG2 in neural stem cells is essential for ciliary neurotrophic factor-induced astrocyte differentiation. *J Cell Biol* **166**: 963–8.

Setty M, Tadmor MD, Reich-zeliger S, Angel O, Salame TM, Kathail P, Choi K, Bendall S, Friedman N, Pe D. 2016. Articles Wishbone identifies bifurcating developmental trajectories from single-cell data. *Nat Biotechnol* **34**: 614–637.

Shcherbo D, Murphy CS, Ermakova G V, Solovieva E a, Chepurnykh T V, Shcheglov AS, Verkhusha V V, Pletnev VZ, Hazelwood KL, Roche PM, et al. 2009. Far-red fluorescent tags for protein imaging in living tissues. *Biochem J* **418**: 567–574.

Shimojo H, Isomura A, Ohtsuka T, Kori H, Miyachi H, Kageyama R. 2016. Oscillatory control of Delta-like1 in cell interactions regulates dynamic gene expression and tissue morphogenesis. *Genes Dev* **30**: 102–116.

Shimojo H, Ohtsuka T, Kageyama R. 2011. Dynamic expression of notch signaling genes in neural stem/progenitor cells. *Front Neurosci* **5**: 78.

Shimojo H, Ohtsuka T, Kageyama R. 2008. Oscillations in Notch Signaling Regulate Maintenance of Neural Progenitors. *Neuron* **58**: 52–64.

Shin J, Berg DA, Christian KM, Shin J, Berg DA, Zhu Y, Shin JY, Song J, Bonaguidi MA. 2015. Single-Cell RNA-Seq with Waterfall Reveals Molecular Cascades underlying Adult Neurogenesis Resource Single-Cell RNA-Seq with Waterfall Reveals Molecular Cascades underlying Adult Neurogenesis. *Stem Cell* **17**: 360–372.

Skaggs K, Martin DM, Novitch BG. 2011. Regulation of spinal interneuron development by the Olig-related protein Bhlhb5 and Notch signaling. *Development* **138**: 3199–3211.

Son EY, Ichida JK, Wainger BJ, Toma JS, Rafuse VF, Woolf CJ, Eggan K. 2011. Conversion of mouse and human fibroblasts into functional spinal motor neurons. *Cell Stem Cell* **9**: 205–218.

Stasiulewicz M, Gray SD, Mastromina I, Silva JC, Bjorklund M, Seymour PA, Booth D, Thompson C, Green RJ, Hall EA, et al. 2015. A conserved role for Notch signaling in priming the cellular response to Shh through ciliary localisation of the key Shh transducer Smo. *Development* **142**: 2291–2303.

Stathopoulos A, Levine M. 2005. Genomic regulatory networks and animal development. *Dev Cell* **9**: 449–462.

Stifani N. 2014. Motor neurons and the generation of spinal motor neuron diversity. *Front Cell Neurosci* **8**: 293.

Sugimori M, Nagao M, Bertrand N, Parras CM, Guillemot F, Nakafuku M. 2007. Combinatorial actions of patterning and HLH transcription factors in the spatiotemporal control of neurogenesis and gliogenesis in the developing spinal cord. *Development* **134**: 1617–29.

Sun Y, Meijer DH, Alberta JA, Mehta S, Kane MF, Tien AC, Fu H, Petryniak MA, Potter GB, Liu Z, et al. 2011. Phosphorylation state of Olig2 regulates proliferation of neural progenitors. *Neuron* **69**: 906–917.

Szymczak AL, Workman CJ, Wang Y, Vignali KM, Dilioglou S, Vanin EF, Vignali DA. 2004. Correction of multi-gene deficiency in vivo using a single “self-cleaving” 2A peptide-based retroviral vector. *Nat Biotechnol* **22**: 589–594.

Takebayashi H, Nabeshima Y, Yoshida S, Chisaka O, Ikenaka K, Nabeshima YI. 2002. The basic helix-loop-helix factor Olig2 is essential for the development of motoneuron and oligodendrocyte lineages. *Curr Biol* **12**: 1157–1163.

Takebayashi K, Sasai Y, Sakai Y, Watanabe T, Nakanishi S, Kageyama R. 1994. Structure, chromosomal locus, and promoter analysis of the gene encoding the mouse helix-loop-helix factor HES-1. Negative autoregulation through the multiple N box elements. *J Biol Chem* **269**: 5150–5156.

Tan GC, Mazzoni EO, Wichterle H. 2016. Iterative Role of Notch Signaling in Spinal Motor Neuron Diversification. *Cell Rep* **16**: 907–916.

Tanabe Y, William C, Jessell TM. 1998. Specification of motor neuron identity by the MNR2 homeodomain protein. *Cell* **95**: 67–80.

Thaler JP, Koo SJ, Kania A, Lettieri K, Andrews S, Cox C, Jessell TM, Pfaff SL. 2004. A Postmitotic Role for Isl-Class LIM Homeodomain Proteins in the Assignment of Visceral Spinal Motor Neuron Identity. *Neuron* **41**: 337–350.

Trapnell C, Cacchiarelli D, Grimsby J, Pokharel P, Li S, Morse M, Lennon NJ, Livak KJ, Mikkelsen TS, Rinn JL. 2014. The dynamics and regulators of cell fate decisions are revealed by pseudotemporal ordering of single cells. *Nat Biotechnol* **32**: 381–386.

Treutlein B, Lee QY, Camp JG, Mall M, Koh W, Ali S, Shariati M, Sim S, Neff NF, Skotheim JM, et al. 2016. Dissecting direct reprogramming from fibroblast to neuron using single-cell RNA-seq. *Nature* **534**: 391–395.

Velasco S, Ibrahim MM, Kakumanu A, Garipler G, Aydin B, Al-Sayegh MA, Hirsekorn A, Abdul-Rahman F, Satija R, Ohler U, et al. 2016. A Multi-step Transcriptional and Chromatin State Cascade Underlies Motor Neuron Programming from Embryonic Stem Cells. *Cell Stem Cell*.

Xiang C, Baubet V, Pal S, Holderbaum L, Tatard V, Jiang P, Davuluri R V, Dahmane N. 2011. RP58 / ZNF238 directly modulates proneurogenic gene levels and is required for neuronal differentiation and brain expansion. *Cell Death Differ* **19**: 692–702.

Zhou Q, Anderson DJ. 2002. The bHLH transcription factors OLIG2 and OLIG1 couple neuronal and glial subtype specification. *Cell* **109**: 61–73.

FIGURE LEGENDS

Figure 1: Characterization of MN differentiation from ESCs

(A) Scheme outlining the differentiation protocol. ESCs are plated in N2B27 + FGF for two days, before being exposed to N2B27 + FGF/CHIR, resulting in the production of neuromesodermal progenitors (NMPs) at D3. Cells are subsequently exposed to retinoic acid (RA) and SAG to promote differentiation into ventral NPs and MNs.
(B, C) Expression of NP (Pax6, Olig2, Nkx2.2, Sox1) and MN (Isl1/2) markers between D4-7 in differentiating ESCs.
(D) RT-qPCR analysis of *Irx3*, *Pax6*, *Nkx6.1*, *Olig2* and *Nkx2.2* expression from D3-7 reveals progressive ventralization in response to increasing duration of Shh signaling.
(E) MN induction after D5 revealed by RT-qPCR analysis of *Sox1*, *Ngn2*, *Isl1* and *Tubb3*.
Scale bars = 40 μm.

Figure 2: Reconstruction of transcriptional changes during MN differentiation

(A) Identification of NP cell states using hierarchical clustering of gene expression profiles of the individual cells
(B) Cell state graph constructed from minimum spanning trees, color coded for the cell populations identified in Fig. 2A. Stars indicate start and end cells for the reconstruction of transcriptional changes along pseudotime. Shading of edges between cells indicates how often the edge was used in the reconstruction of gene expression along pseudotime (see Analytical Supplement).
(C) Cell state graph color coded for expression levels of *Irx3*, *Olig2*, *Fabp7*, *Ngn2*, *Isl1* and *Chat*.
(D) Inferred changes in gene expression over pseudotime from 9000 shortest paths connecting start and end cells (stars in B). Each shortest path was resampled to a length of 40 pseudo-timepoints to enable statistical measurements of gene expression. Cell IDs color coded according to cell states in A. Quantification of the global rate of change in gene expression identifies three metastable states (light gray) separated by transition states during which the rate of change in gene expression is increased (dark gray).
(E) Gene expression profiles along pseudotime for NP TFs (*Irx3*, *Pax6*, *Nkx6.1* and *Olig2*), gene associated with the transition to MNs (*Ngn2*, *Lhx3* and *Neurod4*) and MN markers (*Isl1/2*, *Tubb3* and *Chat*).

(F) Levels of gene expression for *Hes1/5*, *Olig2* and *Ngn2* over pseudotime. Note that *Olig2* expression appears biphasic with a strong upregulation of *Olig2* concommitant to *Ngn2* induction and repression of *Hes1/5* in the transition phase from NP to MN.

Figure 3: Olig2 expression is higher in Ngn2 expressing progenitors in the pMN domain

(A-B'') Staining for Ngn2 (A, B), Olig2 (A', B') merged with Mnx1 (A'', B'') in spinal cords at e9.5 (A-A'') and e10.5 (B-B'').
(C, E) Positive correlation between Olig2 and Ngn2 protein levels in individual nuclei at e9.5 (C, n = 464 nuclei) and e10.5 (E, n = 1078 nuclei).
(D, F) Levels of Olig2, Mnx1 and Ngn2 in individual nuclei throughout the pMN domain at e9.5 (D) and e10.5 (F). Plotting Olig2 versus Mnx1 protein levels reveals a clear differentiation trajectory from Olig2-positive pMN cells to Mnx1-positive MNs. Note that high levels of Ngn2 are only observed in cells with high levels of Olig2 expression. In addition Olig2 protein perdures much longer in Mnx1 positive MNs than Ngn2.
Scale bars = 50 μm.

Figure 4: Quantification of a fluorescent Olig2 reporter reveals a marked upregulation of Olig2 prior to MN differentiation

(A) Design of the Olig2-mKate2 reporter. A 3xNLS-FLAG-mKate2 reporter was fused to the C-terminus of endogenous Olig2 via a T2A self-cleaving peptide.
(B) Western Blot analysis reveals that the targeted allele shows the same expression dynamics and levels as endogenous Olig2. The targeted allele runs at slightly increased molecular weight due to addition of the T2A peptide (see A). Note that both alleles are targeted in this cell line and consequently no protein of wild-type size was detected.
(C-F'') Immunofluorescence for mKate2 with Olig2 (C-C''), Isl1/2 (D-D''), Sox1 (E-E'') and Nkx2.2 (F-F'') at D6 of the differentiations.
(G-J) Quantification of protein levels of mKate2 and Olig2 (G, n = 2851 nuclei), Isl1/2 (H, same dataset as G), Sox1 (I, n = 2049 nuclei) and Nkx2.2 (J, n = 2034 nuclei) in individual nuclei. Note the positive correlation between mKate2 and Olig2 and Isl1/2, and negative correlation between mKate2 and Sox1 and Nkx2.2.
(K) Inhibition of Notch signaling using 10 ng/μl DBZ causes an increase of neurogenesis. Immunofluorescent staining for Olig2, mKate2 and Tubb3 in control or after 24h DBZ treatment at D6 of the differentiation.

(L) Frequency plots of mKate2 fluorescence intensity obtained by flow cytometry reveal a strong increase in the number of mKate2^{HIGH} cells after 24h DBZ treatment.

Scale bars = 25 μm.

Figure 5: Olig2 and Hes are dynamically expressed in the mouse neural tube

(A-D) Expression patterns of Ngn2 (green in A), Olig2 (red in A,C,D), Hes1 (red in B, green in C) and Hes5 (green in B,D) in the neural tube at e10.5. Note the strong repression of Hes1/5 and high level Ngn2 expression in the pMN domain (compare A,B).

(E) Hes5 (green) expression coincides with the expression of high levels of Pax6 (red) in the intermediate neural tube.

(F,G) Hes1 expression (green) is readily detected in both Nkx2.2^{+} p3 progenitors (red in F) and floor plate cells labelled by Foxa2 expression (red in G)

(H-Q') Time course of Olig2 (blue), Hes1 (red), Hes5 (red), and Ngn2 (green) expression in neural tubes between e8.5 and e10.5. Hes1 expression appears to recede from the ventral neural tube upon the onset of Olig2 expression at e8.5 (H) and is thereafter absent from most Olig2+ cells (I-L). Olig2 and Hes5 are initially coexpressed (M,N). Over time, Hes5 expression progressively disappears from the pMN domain (N-Q), and Ngn2 concomitantly increases (N'-Q').

Scale bars = 50 μm.

Figure 6: Repression of Hes1/5 in the pMN domain depends on Olig2 activity

(A-D) Expression of Cre (green in A-D), Olig2 (red in A), Ngn2 (red in B), Hes1 (red in C, grey in C') and Hes5 (red in D, grey in D') in e10.5 Olig2^{Cre} heterozygous embryos.

(E-H) In Olig2$^{Cre/Cre}$ homozygous mutants, Hes1 expands dorsally (G, G') and Hes5 ventrally (H, H') into the pMN domain, marked by Cre expressed from the Olig2 locus. The expansion of Hes1/5 coincides with a loss of the high levels of Ngn2 normally seen in the pMN.

(I) Quantification of Hes1, Hes5 and Ngn2 expression in Olig2^{Cre} heterozygous and homozygous embryos. The overlap between Cre and Hes1/5 significantly increases in Olig2^{Cre} homozygotes while overlap between Ngn2 and Cre is strongly reduced. Plot shows the mean ± SEM from multiple sections collected from 3 to 5 embryos for each group. Each section is represented by a single dot with n = 8-11 for each group. **** $p < 0.0001$, unpaired t-test.

(J) Summary diagram illustrating how Olig2 represses Hes1/5 to promote Ngn2 expression in the pMN domain.

Scale bars = 50 μm.

Figure 7: Olig2 binds to an evolutionary conserved element near Hes5

(A) Identification of an evolutionary conserved element containing an E-box in the vicinity of the *Hes5* genomic locus in chick, mouse and human (Hes5(e1)).

(B) Analysis of Olig2 Chip-Seq data from Kutejova et al. 2016 reveals Olig2 binding sites in the vicinity of the *Hes1* and *Hes5* genes. The peak corresponding to the Hes5(e1) element is highlighted in red.

(C) Electrophoretic mobility shift assays show that both Olig2 and E12 homodimers can individually bind to the Hes5(e1) E-box, and do not form any heterodimeric complexes (lanes 1-4). Positions of the different protein complexes are indicated by colored arrows. Binding depends on the E-box as both proteins fail to bind probes containing an E-box mutation (Hes5(e1ΔE) (lanes 5-7). Olig2 binding to Hes5(e1) can be abolished by the addition of unlabelled Hes5(e1) probes, but not those containing the E-box mutation (lanes 8-14).

(D) Id1 inhibits binding of E12, but not of Olig2 or Ngn2, to the Hes5(e1) element. Olig2, E12 and Ngn2 alone or Ngn2/E12 heterodimers can bind the Hes5(e1) element. Mixing Olig2 or Ngn2 with Id1 does not inhibit their homodimeric binding activities (lanes 2, 5, 8, and 10). In contrast, Id1 strongly inhibits binding of both E12/E12 and Ngn2/E12 complexes (lanes 6 and 10). The addition of E12 without and with Id1 does not affect Olig2 binding efficiency (lanes 2, 4, and 7).

Figure 8: The Hes5(e1) element is required for repression of reporter genes in the pMN domain

(A,B) Co-electroporation of CMV/β-actin::nLacZ and Hes5(e1) reporter plasmids into chick spinal cord. Although electroporation (revealed by β-Gal staining, magenta in A) is uniform along the DV axis, expression of the EGFP-reporter is confined to intermediate parts of neural tube (A,B) and little coexpression of Olig2 and EGFP was detected (B).

(C) Design of Hes5(e1) and Hes5(e1ΔE) reporters. The Hes5(e1) element was cloned in front of β-globin minimal promoter to drive EGFP reporter gene expression. To test the importance of the E-box in the Hes5(e1) element, critical base pairs for Olig2 binding were mutated (red).

(D,E) Co-electroporation of CMV/β-actin::-nLacZ and Hes5(e1ΔE) reporter plasmids into chick spinal cord. In contrast to the Hes5(e1) reporter plasmid, significant coexpression of Olig2 and GFP in the pMN domain is detected (E). Note that E box mutation reduced the basal activity of the reporter, such that longer exposure times were needed to achieve the signals levels seen in the intermediate spinal cord with the nonmutated Hes5(e1) reporter.

(F) Scatter dot plots display the dorsoventral positions of individual cells expressing the Hes5(e1) and Hes5(e1ΔE) reporters relative to CMV/β-actin::-nLacZ and Olig2. Results are aggregated from five representative sections taken from five well-electroporated and stage-matched spinal cords. The Hes5(e1ΔE) reporter exhibits a significant ventral shift in its activity and considerable overlap with Olig2 expression (blue dotted box). Lines and error bars indicate mean and interquartile ranges, respectively. *** p = 0.0005, Mann-Whitney test; ns, not significant, p = 0.6649.

(G) EGFP-expression in Hes5(e1)-nEGFP whole mount embryos at e10.5**.**

(H-H”) Cryosections of Hes5(e1)-nEGFP embryos at e10.5 assayed for GFP, Olig2 and Hes5. EGFP expression colocalizes with Hes5 expression (H”), but not with Olig2 (H).

(I-P) Hes5(e1)-nEGFP expression in *Olig2* heterozygous (I,K,L) and homozygous mutants (J,M,N). In *Olig2* heterozygotes, little nEGFP expression can be detected in the Olig2 expression domain, resulting in a pronounced gap between the expression domains of EGFP, Nkx2.2 and Hes1 (K,L). By contrast, the EGFP, Nkx2.2 and Hes1 expression domains directly abut each other in Olig2 homozygous mutants (M,N).

SUPPLEMENTAL FIGURE LEGENDS

Figure 1-figure supplement 1: Characterization of Hox gene expression in NPs and MNs

(A) RT-qPCR analysis of Hox gene expression levels from D3-7

(B) Hoxc6 expression in MNs characterized by Isl1 and Tubb3 expression from D6-8.

(C) Expression of the somatic MN marker Mnx1 in MNs at D6.

Figure 2-figure supplement 1: Identification of gene modules and cell states by hierarchical clustering of single cell sequencing data

(A) Identification of cell states by hierarchical clustering from 202 cells based on 10 identified gene modules. Genes characteristic for the individual modules are indicated. Boxed region corresponds to the heatmap in Fig. 2A.

(B) Inhibition of Notch signaling, revealed by declining expression levels of *Hes1/5* and expression of the Notch ligand *Dll1* and the pathway inhibitors *Hes6* and *Numbl*, drives the cell state transition from NPs to MNs.

(C) The transition phase from early *Irx3* NPs to *Olig2* NPs correlates with the induction of Shh target genes *Ptch2*, *Gli1*, *Hhip*.

Figure 3-figure supplement 1: Validation of predictions from the pseudotemporal ordering

(A) Sequential expression of Olig2, Ngn2, Lhx3 and Isl1 during MN differentiation revealed by immunofluorescent staining for these markers at D6 of differentiation.

(B,C) Quantification of levels of Olig2, Isl1, Ngn2 (color code in B) and Lhx3 (color code in C) reveals a clear differentiation path from Olig2^{HIGH} cells to MNs and sequential induction of Ngn2 and Lhx3 during this process (n = 2236 nuclei).

(D) Staining for Isl1, Lhx3 and Tubb3 reveals high level of Tubb3 expression in Isl1-positive but not Lhx3-positive MNs at D6 of differentiation. This is consistent with the earlier MN stage of Lhx3 MNs.

(E, F) Most positive and negative Spearman-correlated transcription factors for Olig2 (E) and Ngn2 (F) reveals Zbtb18 (green in E-G) as a novel gene involved in MN formation.

(G) Expression profiles of Olig2, Zbtb18, Ngn2, Neurod4 and Isl1 along pseudotime.

(H-H'') Immunofluorescent staining for Olig2 (H), Zbtb18 (H'), and Ngn2 (H'') at D6 of differentiation.

(I, J) Quantification of levels of Olig2, Ngn2 (I) and Zbtb18 (J) in individual nuclei reveals a good correlation between these markers (n = 1431 nuclei).
(K-M) Analysis of Olig2, Ngn2, and Zbtb18 expression in neural tubes at e9.5 (K), e10.5 (L) and e11.5 (M). Note that Ngn2 and Zbtb18 are expressed in cells with high levels of Olig2 at e9.5 and e10.5, but not at e11.5 (left insets in K-M). In addition, Zbtb18 and Ngn2 are coexpressed in nuclei at the edge of the progenitor domain in dorsal areas of the neural tube at e10.5 (L) and e11.5 (M) (right insets).
Scale bars = 25 μm in (A,D), 10 μm in (H) and insets in K-M, 50 μm in K-M

Figure 4-figure supplement 1: Characterization of the Olig2-mKate2 reporter cell line by flow cytometry and upon Notch inhibition

(A-C) Quantification of mKate2 and Tubb3 fluorescence intensity by flow cytometry at D4-6 of differentiation. Note that high levels of Tubb3 are predominantly detected in mKate2^{HIGH} cells at D6 (C).
(D-F) Correlation between Olig2 and mKate2 levels in individual nuclei quantified from images in Fig. 4C-F. Plots are color coded for levels of Isl1/2 (D), Sox1 (E) and Nkx2.2 (F).
(G) Quantification of the increase in mKate2^{HIGH} cells upon 24h Notch inhibition for 5 experimental repeats. Each repeat consists of the measurement of three independent dishes for control and Notch inhibition from the same differentiation. *** $p < 0.001$, unpaired t-test
(H) Quantification of the percentage of mKate2-positive cells upon Notch inhibition (grey) relative to untreated control differentiations (black). Notch inhibition does not cause an overall change in the number of mKate2 positive cells. * $p < 0.05$; ** $p < 0.01$, unpaired t-test
(I) Quantification of mKate2 and Tubb3 fluorescence intensity by flow cytometry upon 24h Notch inhibition. Note that most mKate2^{HIGH} cells differentiated into MNs (compare to Figure 4-figure supplement 1C).
(J-L) RT-qPCR quantification of expression levels of progenitor markers *Sox1*, *Hes5*, *Hes1* and *Pax6* (J), neurogenesis markers *Olig2*, *Ngn2*, *Zbtb18* and *Pou3f2* (K) and MN markers *Tubb3* and *Isl1* (L) upon Notch inhibition (grey) and in untreated controls (black). Note that *Olig2* expression increases in contrast to other progenitor markers after 12h of Notch inhibition.

Figure 6-figure supplement 1: Ectopic Olig2 suppresses Hes/Hairy expression in the chick spinal cord

(A-J) Electroporation of myc-tagged Olig2 and an Olig2-bHLH-Engrailed repressor domain fusion protein in chick neural tubes represses expression of the Hes5 homologues *Hes5-1* to *Hes5-3* (B-D; G-I) and the Hes1 homologue

Hairy1 (E,J). '+' indicates transfected side of the spinal cords. Scale bars = 50 μm. Results are representative of > 5 successfully transfected embryos collected from two or more experiments.

Figure 7-figure supplement 1: Olig2 and Ngn2 bind to Hes5(e1) *in vivo*

Both Olig2 and Ngn2 antibodies precipitate the Hes5(e1) genomic element from ES cell-derived motor neuron progenitors, but not Hes5(e2), an unrelated genomic element 3' to the Hes5 coding exons that also contains an E-box. Fold enrichment relative to normal rabbit sera or purified IgG is displayed. **** $p < 0.0001$; ** $p < 0.01$, Mann-Whitney test.

Table S1: List of qPCR primers

Gene	Forward primer	Reverse primer
Hes1	GGCGAAGGGCAAGAATAAATG	GTGCTTCACAGTCATTTCCAG
Hes5	CCAAGGAGAAAAACCGACTG	AACTCCTGCTCCAGCAGCA
Hes5(e1)	CTGCTTCTGAATGAATGAGGGCGG	AGCAGACGAGCCCTTTATTGCTCT
Hes5(e2)	AGATGGCTCAGCGGTTAAGAG	CCATGTGGTTGCTGGGATTTG
Hoxb1	AGAGGCTGGCTTACGAGAC	GGTTGAGGCTTGCTTGAGG
Hoxb4	AGCACGGTAAACCCCAATTACG	CGCGTCAGGTAGCGATTGTAG
Hoxb6	AAGAGCGTGTTCGGAGAG	TGAAATTCCTTCTCCAGCTC
Hoxb8	CAGCTCTTTCCCTGGATG	CACTTCATTCTCCGATTCTG
Hoxb9	TAATCAAAGAGCTGGCTACG	CCCTGGTGAGGTACATATTG
Hoxc6	CAGGTAAAGGCAAAGGGATG	ATAGGCGGTGGAATTGAGG
Hoxc9	AGCCGACAGAGACAGATTAC	AATGCCAGTCCCAGAAGC
Irx3	GGAGAGTGGAACAGATCGCT	CTGATAAGACCAGAGCAGCGT
Isl1	TATCAGGTTGTACGGGATCAAA	CTACACAGCGGAAACACTCG
Ngn2	AACTGGAGTGCCTTGGAGTC	CGAGTCTCGTGTGTTGTCGT
Nkx2.2	CAGCCTCATCCGTCTCAC	TCACCTCCATACCTTTCTCC
Nkx6.1	CCCGGAGTGATGCAGAGT	GAACGTGGGTCTGGTGTGTT
Olig2	AGACCGAGCCAACACCAG	AAGCTCTCGAATGATCCTTCTTT
Pax6	ACCCGGCAGAAGATCGTAG	TTTGCATCTGCATGGGTCT
Pou3f2	AGCTTCCCAATGCTCAAAGT	GCAGTGCAAATTCTTGTGGT
Sox1	AGCGTGCCTTTGATTTCTCT	GGGATAAGACCTGGGTGAGA
Tubb3	CAACAGCACGGCCATCCAGG	CTTGGGGCCCTGGGCCTCCGA
Zbtb18	GTTCGGATAAAGTCGAGAGCC	CCCTTTTGCTGGGTAGAATGT

Supplementary file 1: Gene modules describing the biological processes represented in the scRNA-seq dataset

Supplementary file 2: GO annotations of the 22 gene modules (pval < 0.05)

SOURCE DATA LEGENDS

Figure 1D,E - source data: qPCR analysis displayed in Figure 1D,E

Figure 2 – source data: Gene expression data from RNA-Seq and complementary information. Spreadsheet showing the transcriptome-wide normalized gene levels in counts per million (CPM) for all 202 cells contained in the D4, D5 and D6 datasets, as well as along pseudotime (41 pseudotime points). In addition, the row indicates the cell clusters shown in Figure 2B and Figure 2-figure supplement 1A ('ep' for Early Progenitor, 'mnp' for Motor Neuron Progenitors, 'ohp' for Olig2 High Progenitors, 'emn' for Early Motor Neurons, 'lmn' for Late Motor Neurons, 'gp' for 'Glial Progenitors', 'pm_1'/'pm_2' for Paraxial Mesoderm and 've_1'/'ve_2' for Vascular Endothelium). The second and third row indicates the spatial coordinates of the cells displayed in the cell state graphs. The fourth row indicates the gene variation displayed in Figure 2E,D and Figure 2-figure supplement 1C.

Figure 3C,D – source data: Intensity measurements of Olig2, Mnx1 and Ngn2 in the pMN domain of spinal cords at e9.5 to generate plots in Figure 3C,D

Figure 3E,F – source data: Intensity measurements Olig2, Mnx1 and Ngn2 in the pMN domain of spinal cords at e10.5 to generate plots in Figure 3E,F

Figure 4G,H and S4D – source data: Intensity measurements of Olig2, mKate2 and Islet1/2 to generate plots in Figures 4G,H and Figure 4-figure supplement 1D

Figure 4I and S4E – source data: Intensity measurements of Olig2, mKate2 and Sox1 to generate plots in Figures 4I and Figure 4-figure supplement 1E

Figure 4J and S4F – source data: Intensity measurements of Olig2, mKate2 and Nkx2.2 to generate plots in Figures 4J and Figure 4-figure supplement 1F

Figure 6I – source data: Quantification of Hes1, Hes5 and Ngn2 expression in Olig2^{Cre} heterozygous and homozygous embryos

Figure 8F – source data: Analysis of the dorsoventral positions of individual cells expressing the Hes5(e1) and Hes5(e1ΔE) reporters relative to CMV/β-actin::-nLacZ and Olig2

Figure S1A – source data: qPCR analysis displayed in Figure 1-figure supplement 1A

Figure S3B – source data: Intensity measurements of Olig2, Ngn2 and Islet1 to generate the plots shown in Figure Figure 3-figure supplement 1B

Figure S3C – source data: Intensity measurements of Olig2, Lhx3 and Islet1 to generate the plots shown in Figure Figure 3-figure supplement 1C

Figure S4J,K,L – source data: qPCR analysis displayed in Figure Figure 4-figure supplement 1J,K,L

Figure S7 – source data: ChiP-qPCR analysis of Olig2 binding to Hes5(e1)

ANALYTICAL SUPPLEMENT

RNA sequences alignment and pre-processing

Sequences were aligned to the Ensemble mouse genome GRCm38 using Tophat2 (Kim et al., 2013) and counted with HTSeq-count. Cell debris and doublets were removed from the data by inspecting miscroscope images of the microfluidic chips. Low-quality libraries were excluded from the 236 sequenced single-cell transcriptomes if their transcript abundance was less than 10^6 reads and the number of expressed genes was less than one thousand. The 202 retained libraries (25 cells from D4, 68 cells from D5 and 109 cells from D6) were normalized to read counts per million (CPM). Genes with counts in less than 3 cells or annotated as pseudogenes were excluded from the analysis.

Cell state identification

To identify the cell states in the dataset, we applied a two-stage strategy aimed at selecting the gene modules demonstrating relevant and concerted patterns of expression. First, we took a data-driven approach to characterize the different modules of interacting genes. From the initial set of 13196 expressed genes, we selected the 2287 genes that showed Spearman correlation ($r > 0:4$) with at least two other genes. The correlated genes were grouped into 127 gene modules by performing a hierarchical clustering using the Euclidean distance of the z-scored log-transformed gene levels and Ward's agglomeration criterion (Ward, 1963). The number of modules was selected by determining the “elbow" position in the curve representing the total within-module gene level variation per number of modules. Gene modules were removed according to two criteria: insufficient number of cells expressing the comprised genes and inconsistent gene pattern in these cells. Both criteria were assessed by binarizing gene expression levels using an parameter-free adaptive thresholding method (R function binarize.array from the ArrayBin package). For each cell, we obtained an average expression level per module by averaging the z-scored log-transformed expression levels of all genes belonging to the module. Each of the 127 average expression level distributions were binarized independently. A cell was considered expressing a gene module if the associated boolean value was true. Modules having less than 5 cells expressing it were excluded. The second criterion was designed to verify that cells expressing a gene module were showing consistently high levels over most of the genes composing the module. We binarized the z-scored log-transformed expression levels of all genes independently. Then, for each module, we calculated the ratio of boolean values in cells expressing the module (as defined above). We excluded modules where less than half of these boolean values were true. 22 modules comprising 1064 genes were retained.

Second, functional annotation of the gene modules revealed the global and unbiased description of the biological processes represented in the dataset (see Supplementary files 1 and 2 showing the genes modules and their associated GO terms). To focus on cell type characterization, we selected the 10 modules comprising the GO terms associated with embryonic development, i.e. nervous system development (GO:0007399), skeletal system development (GO:0001501), angiogenesis (GO:0001525), cell differentiation (GO:0030154).

Cell population clustering

In order to define the cell populations present in the dataset, we performed a hierarchical clustering (Ward's agglomeration criterion) of the Euclidean distances between cells using the z-scored log-transformed expression levels of the 545 genes included in the 10 selected modules (Figures 2A and Figure 2-figure supplement 1A). The 4 cell clusters containing vascular endothelial and mesodermal cells and the 5 associated gene modules were excluded from the subsequent analysis. 5 gene modules and 306 genes were retained.

Single-cell state graph

To investigate the dynamical changes of the transcriptional profile as cells differentiate, we developed a method to relate each cell to its closest neighbours in expression space. Unlike cluster analysis which aims to partition cells into groups with similar characteristics, hence breaking the continuity of cell state differentiation, we set out to generate graphs that connect individual cells without requiring the definition of groups. These can reveal the differentiation trajectories and intermediate states that link the clusters of similar cells (the “clustered" populations).

Using the log-transformed expression levels in the 306 genes space, we first calculated the Euclidean distance matrix between each cell and hence constructed a complete weighted graph of cell similarity D. In (Trapnell et al., 2014, Camp et al., 2015), a minimum spanning tree algorithm (MST) was used to extract the subset of cell-cell edges, which forms the backbone of differentiation branches. While MSTs ensure that all cells are connected, they are also sensitive to noise, making the local structure sensitive to small changes in the data (Zemel and Carreira-Perpinan, 2005). To improve robustness to noise of MSTs, we constructed a consensus graph which combines multiple perturbed minimum spanning trees (pMST). Each pMST is obtained by calculating a MST from the cell dissimilarity matrix D with a certain ratio j of its elements set to a very large value (j=20%), hence forbidding the recruitment of the associated edges. Individual pMST are merged by summing their adjacency matrix A into a matrix storing the occurrences of each edge. We then exclude rarely used edges by clustering the non-null edge occurrence distribution using the Fisher method (Fisher,1958) and removing all edges belonging to the first class. This leaves edges that are used repeatedly in multiple permutations and therefore represent good choices for inclusion in MST graphs. The perturb-and-merge algorithm works iteratively until convergence in the number of included edges. The graph visualization shown in Figure 2B and 2C were obtained by projecting the graph into 2D where the positions of each cell (node) in the graph were initially random and then adjusted using an iterative force-based layout algorithm, ForceAtlas2 (Jacomy et al., 2014).

Pseudo-temporal ordering

One of the advantages of generating a single-cell state graph is the possibility to infer a pseudotemporal ordering of the gene expression by following the gene expression implied by the spanning tree. The strategy we used was to identify two terminal cell populations, early and a late and then find the K-shortest paths that connect each pair of early and late cells (Martins and Pascoal, 2003). The early population was specified by selecting the 3 cells expressing a combination of highest Irx3 level and lowest Tubb3 level, and the late population by selecting the 3 cells expressing the highest Tubb3 level. A thousand k-shortest paths were generated for each of the 9 pairs of early and late cells. The resulting 9000 paths did not necessarily have the same length hence, in order to average gene expression along all paths, each of the 9000 paths was rescaled to the same length. The path rescaling was performed by repeating each cell ids so that the total path length would match a constant value set to 41 pseudotime points. The 9000 equally-sized paths then provided a list of 9000 cell ids for each of the 41 pseudotime points. These lists allowed the calculation of various measurements along the pseudotime scale. In particular, Figures 2E, 2F, Figure 2-figure supplement 1B and Figure 2-figure supplement 1C show the mean value of the 9000 log-transformed gene levels for each of the 41 time points. All the pseudotemporal dynamics were smoothed using a local polynomial regression fit (R function loess with span=0.5)

Gene variation and dynamical states

Quantification of the metastable states and transition phases were obtained by calculating the global gene variation along pseudotime. To do so, we identified the 2466 genes with higher dispersion, i.e. higher ratio of variance over mean as described in (Satija et al., 2015), and with an average expression level higher than 10 CPM to avoid taking into account low-level gene's variation. The absolute value of the first derivative of these genes was averaged to define the gene variation (Figures 2D, 2E and Figure 2-figure supplement 1B).

After applying differentiation-and-smoothing twice to gene variation (smoothing with local polynomial regression fit), we obtained a profile showing positive values for periods of higher gene variation and negative values for periods of lower gene variation, hence defining the dynamical states along pseudotime. This operation is equivalent to applying a low-pass Savitzky-Golay filter to the gene variation signal.

References

Camp, J. G., Badsha, F., Florio, M., Kanton, S., Gerber, T., Wilsch-Bräuninger, M., Lewitus, E., Sykes, A., Hevers, W., Lancaster, M., Knoblich, J. A., Lachmann, R., Pääbo, S., Huttner, W. B. and Treutlein, B. (2015). Human cerebral organoids recapitulate gene expression programs of fetal neocortex development. Proceedings of the National Academy of Sciences of the United States of America 112, 15672.

Fisher, W. (1958). On Grouping for Maximum Homogeneity. Journal of the American Statistical Association 53, 789-798.

Jacomy, M., Venturini, T., Heymann, S., Bastian, M., Diminescu, D., Batagelj, V., Mrvar, A., Davidson, R., Harel, D., Hu, Y., Kamada, T., Kawai, S., Noack, A., Newman, M., Krzywinski, M., Birol, I., Jones, S., Marra, M., Eades, P., Fruchterman, T., Reingold, E., Kleinberg, J., Barnes, J., Hut, P. and Purchase, H. (2014). ForceAtlas2, a Continuous Graph Layout Algorithm for Handy Network Visualization Designed for the Gephi Software. PLoS ONE 9, e98679.

Kim, D., Pertea, G., Trapnell, C., Pimentel, H., Kelley, R., Salzberg, S. L., Mortazavi, A., Williams, B., McCue, K., Schaeffer, L., Wold, B., Pei, B., Sisu, C., Frankish, A., Howald, C., Habegger, L., Mu, X., Harte, R., Balasubramanian, S., Tanzer, A., Diekhans, M., Reymond, A., Hubbard, T., Harrow, J., Gerstein, M., Roberts, A., Trapnell, C., Donaghey, J., Rinn, J., Pachter, L., Trapnell, C., Pachter, L., Salzberg, S., Wu, T., Nacu, S., Grant, G., Farkas, M., Pizarro, A., Lahens, N., Schug, J., Brunk, B., Stoeckert, C., Hogenesch, J., Pierce, E., Dobin, A., Davis, C., Schlesinger, F., Drenkow, J., Zaleski, C., Jha, S., Batut, P., Chaisson, M., Gingeras, T., Wang, K., Singh, D., Zeng, Z., Coleman, S., Huang, Y., Savich, G., He, X., Mieczkowski, P., Grimm, S., Perou, C., MacLeod, J., Chiang, D., Prins, J., Liu, J., Zhang, Z., Harrison, P., Liu, Y., Gerstein, M., Kalyana-Sundaram, S., Kumar-Sinha, C., Shankar, S., Robinson, D., Wu, Y., Cao, X., Asangani, I., Kothari, V., Prensner, J., Lonigro, R., Iyer, M., Barrette, T., Shanmugam, A., Dhanasekaran, S., Palanisamy, N., Chinnaiyan, A., Chen, R., Mias, G., Li-Pook-Than, J., Jiang, L., Lam, H., Miriami, E., Karczewski, K., Hariharan, M., Dewey, F., Cheng, Y., Clark, M., Im, H., Habegger, L., Balasubramanian, S., O'Huallachain, M., Dudley, J., Hillenmeyer, S., Haraksingh, R., Sharon, D., Euskirchen, G., Lacroute, P., Bettinger, K., Boyle, A., Kasowski, M., Grubert, F., Seki, S., Garcia, M., Whirl-Carrillo, M., Gallardo, M., Blasco, M., Xing, J., Zhang, Y., Han, K., Salem, A., Sen, S., Hu_, C., Zhou, Q., Kirkness, E., Levy, S., Batzer, M., Jorde, L., Levy, S., Sutton, G., Ng, P., Feuk, L., Halpern, A., Walenz, B., Axelrod, N., Huang, J., Kirkness, E., Denisov, G., Lin, Y., MacDonald, J., Pang, A., Shago, M., Stockwell, T., Tsiamouri, A., Bafna, V., Bansal, V., Kravitz, S., Busam, D., Beeson, K., McIntosh, T., Remington, K., Abril, J., Gill, J., Borman, J., Rogers, Y., Frazier, M., Scherer, S., Strausberg, R., Langmead, B., Salzberg, S., Kim, D., Salzberg, S., Langmead, B., Trapnell, C., Pop, M., Salzberg, S., Griebel, T., Zacher, B., Ribeca, P., Raineri, E., Lacroix, V., Guigo, R. and Sammeth, M. (2013). TopHat2: accurate alignment of transcriptomes in the presence of insertions, deletions and gene fusions. Genome Biology 14, R36.

Martins, E. and Pascoal, M. (2003). A new implementation of Yen’s ranking loopless paths algorithm. Quarterly Journal of the Belgian, French and Italian Operations Research Societies 1, 121-133.

Satija, R., Farrell, J. A., Gennert, D., Schier, A. F. and Regev, A. (2015). Spatial reconstruction of single-cell gene expression data. Nature Biotechnology 33, 495-502.

Trapnell, C., Cacchiarelli, D., Grimsby, J., Pokharel, P.,Li, S., Morse, M., Lennon, N. J., Livak, K. J., Mikkelsen, T. S. and Rinn, J. The dynamics and regulators of cell fate decisions are revealed by pseudotemporal ordering of single cells. Nature biotechnology 32 , 381-386.

Ward, J. H. (1963). Hierarchical Grouping to Optimize an Objective Function. Journal of the American Statistical Association 58, 236-244.

Zemel, R. S. and Carreira-Perpinan, M. A. (2005). Proximity Graphs for Clustering and Manifold Learning. In Advances in Neural Information Processing Systems 17, (Saul, L. K., Weiss, Y. and Bottou, L., eds), pp. 225-232. MIT Press.

Sagner et al. - Figure 1

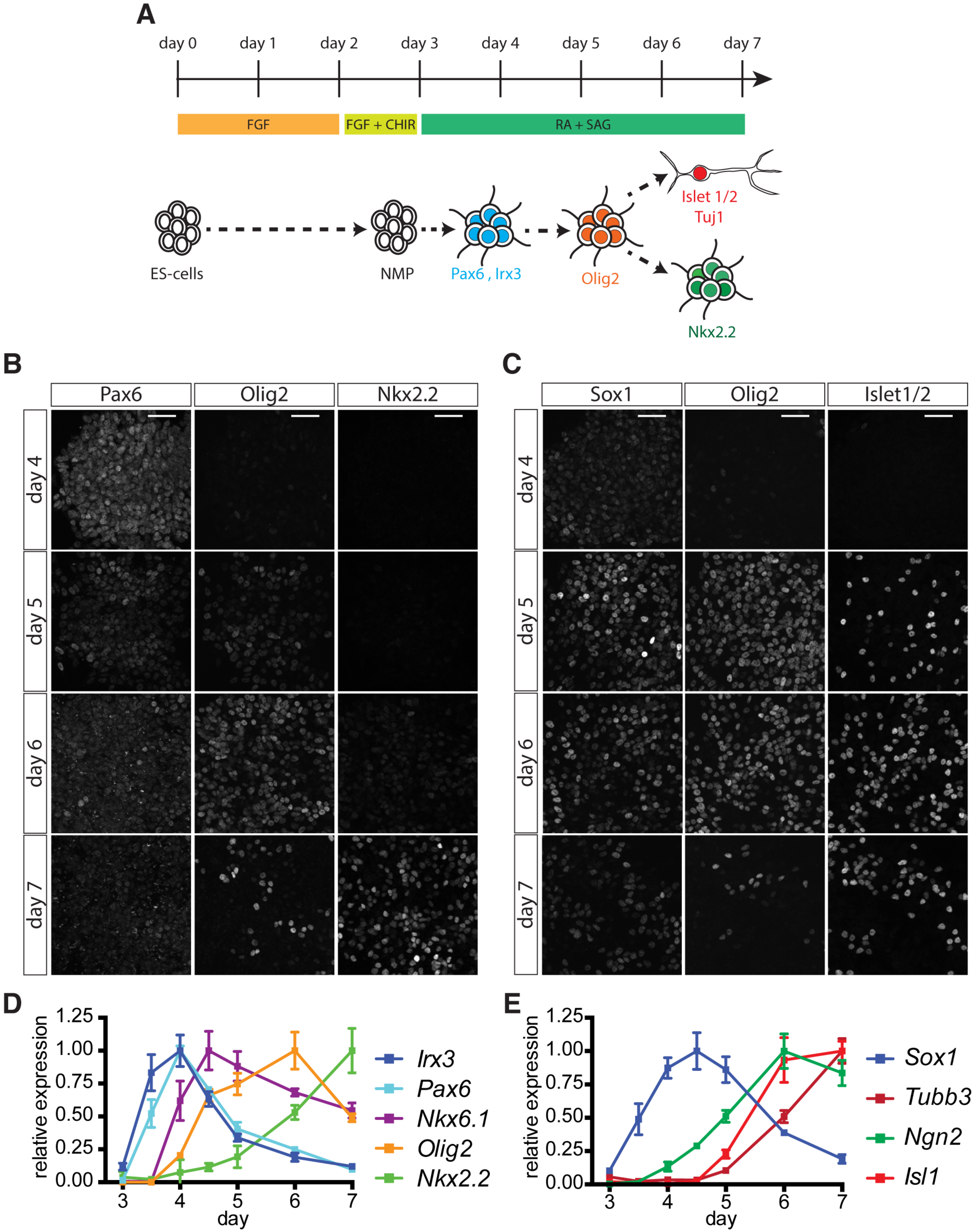

Sagner et al. - Figure 2

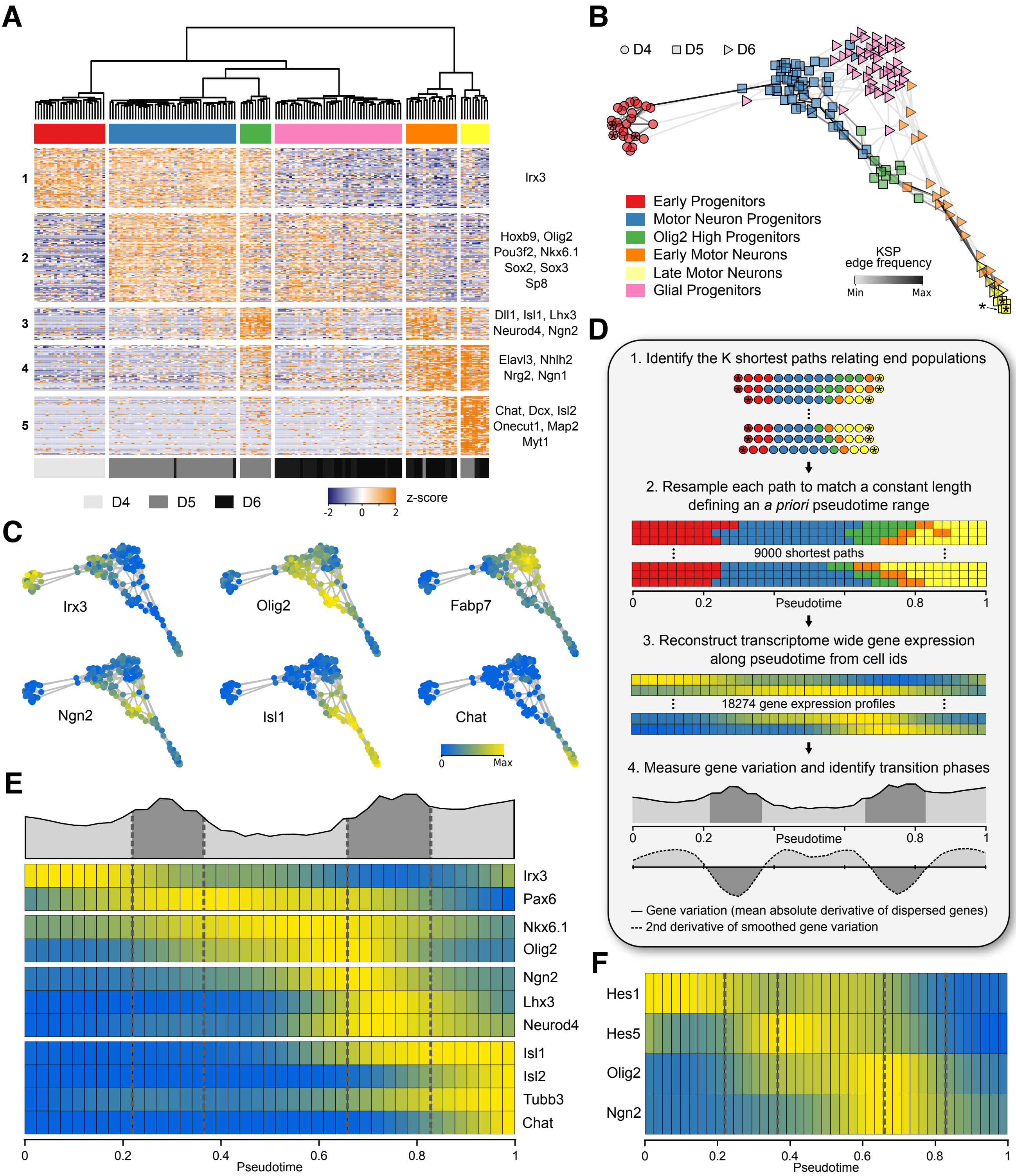

Sagner et al. - Figure 3

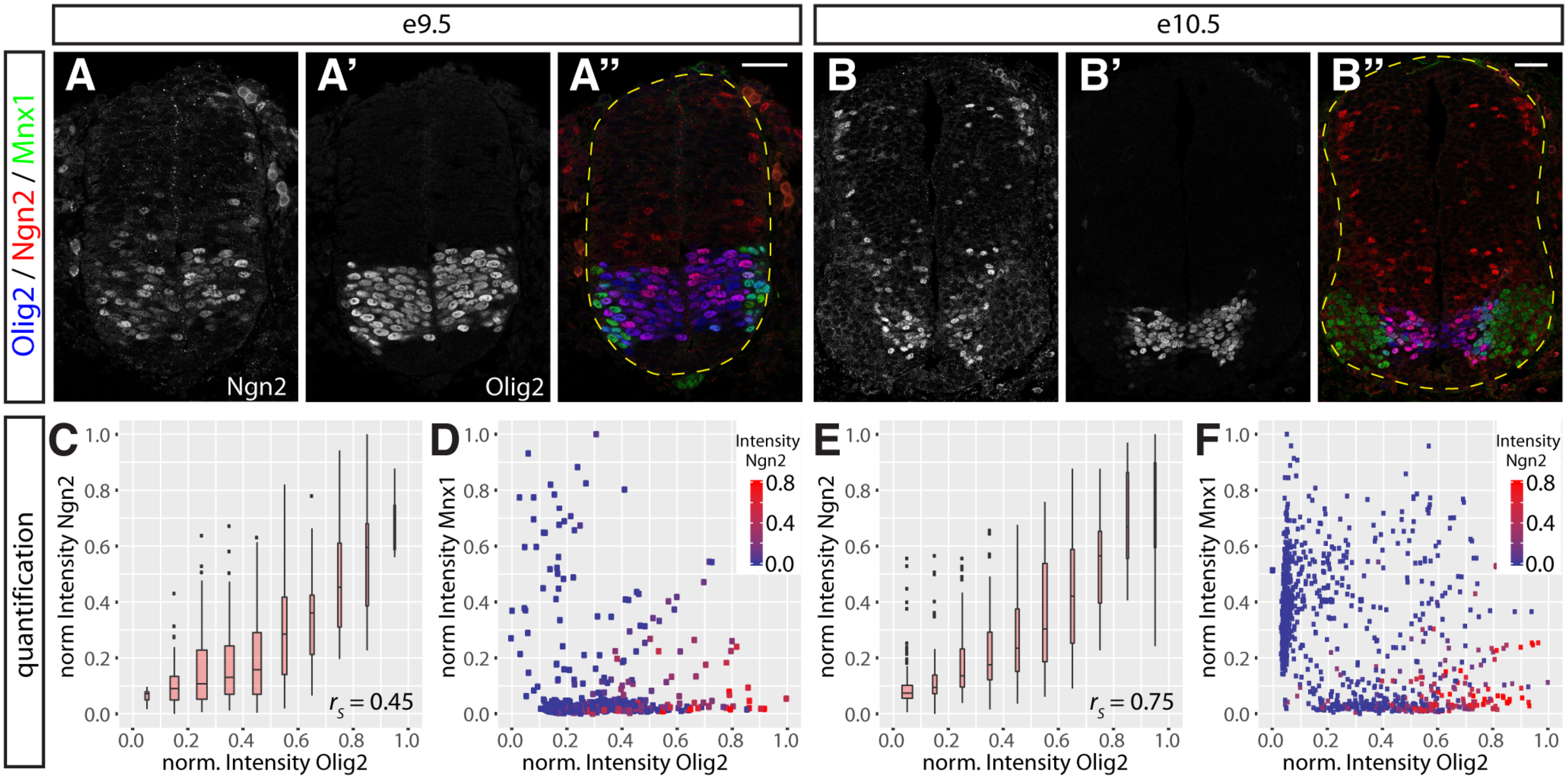

e9.5
e10.5
Olig2 / Ngn2 / Mnx1
A
A'
A''
Ngn2
Olig2
B
B'
B''
quantification
C
norm Intensity Ngn2
norm. Intensity Olig2
$r_S = 0.45$
D
norm Intensity Mnx1
norm. Intensity Olig2
Intensity Ngn2
0.8
0.4
0.0
E
norm Intensity Ngn2
norm. Intensity Olig2
$r_S = 0.75$
F
norm Intensity Mnx1
norm. Intensity Olig2
Intensity Ngn2
0.8
0.4
0.0
0.0 0.2 0.4 0.6 0.8 1.0

Sagner et al. - Figure 4

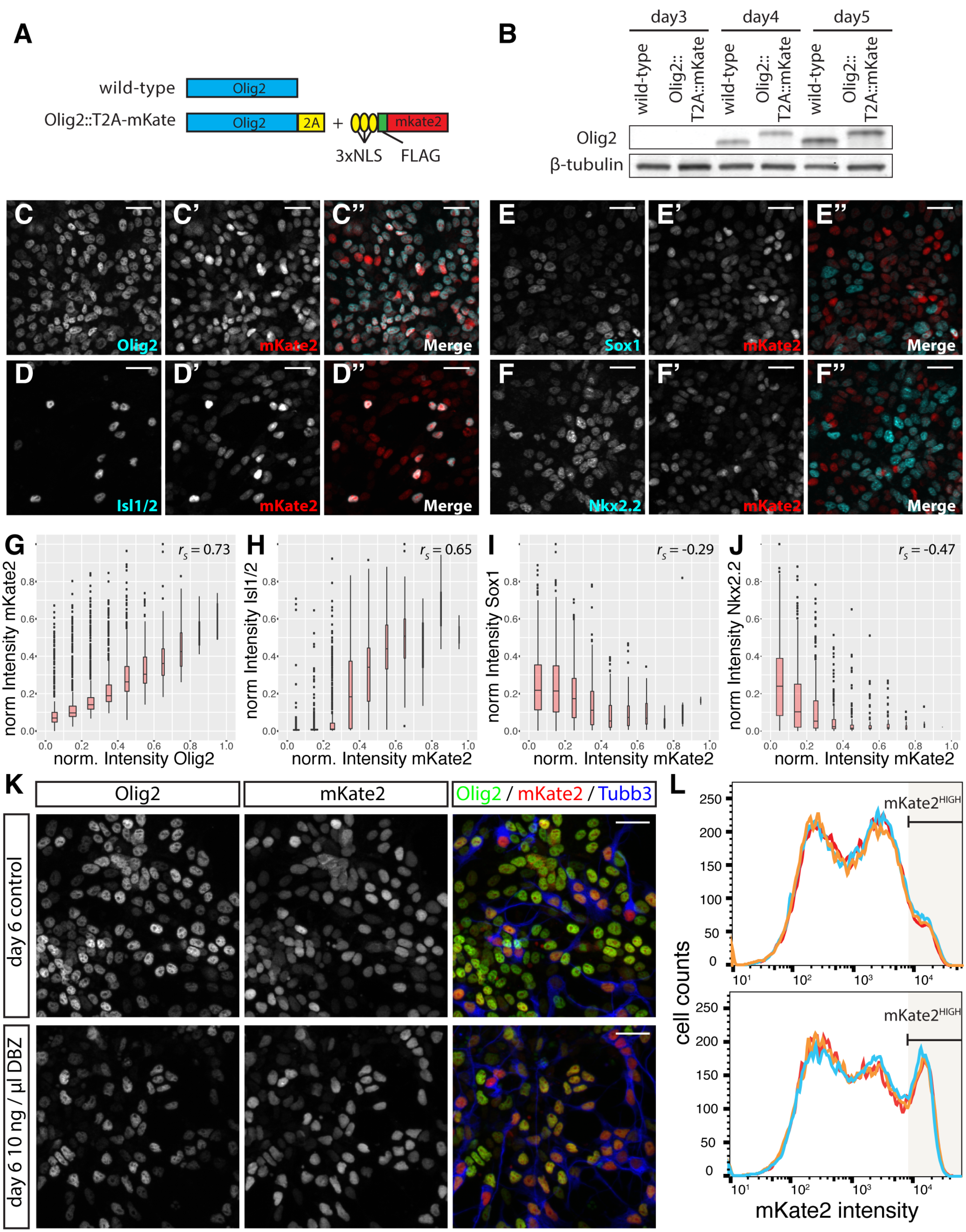

Sagner et al. - Figure 5

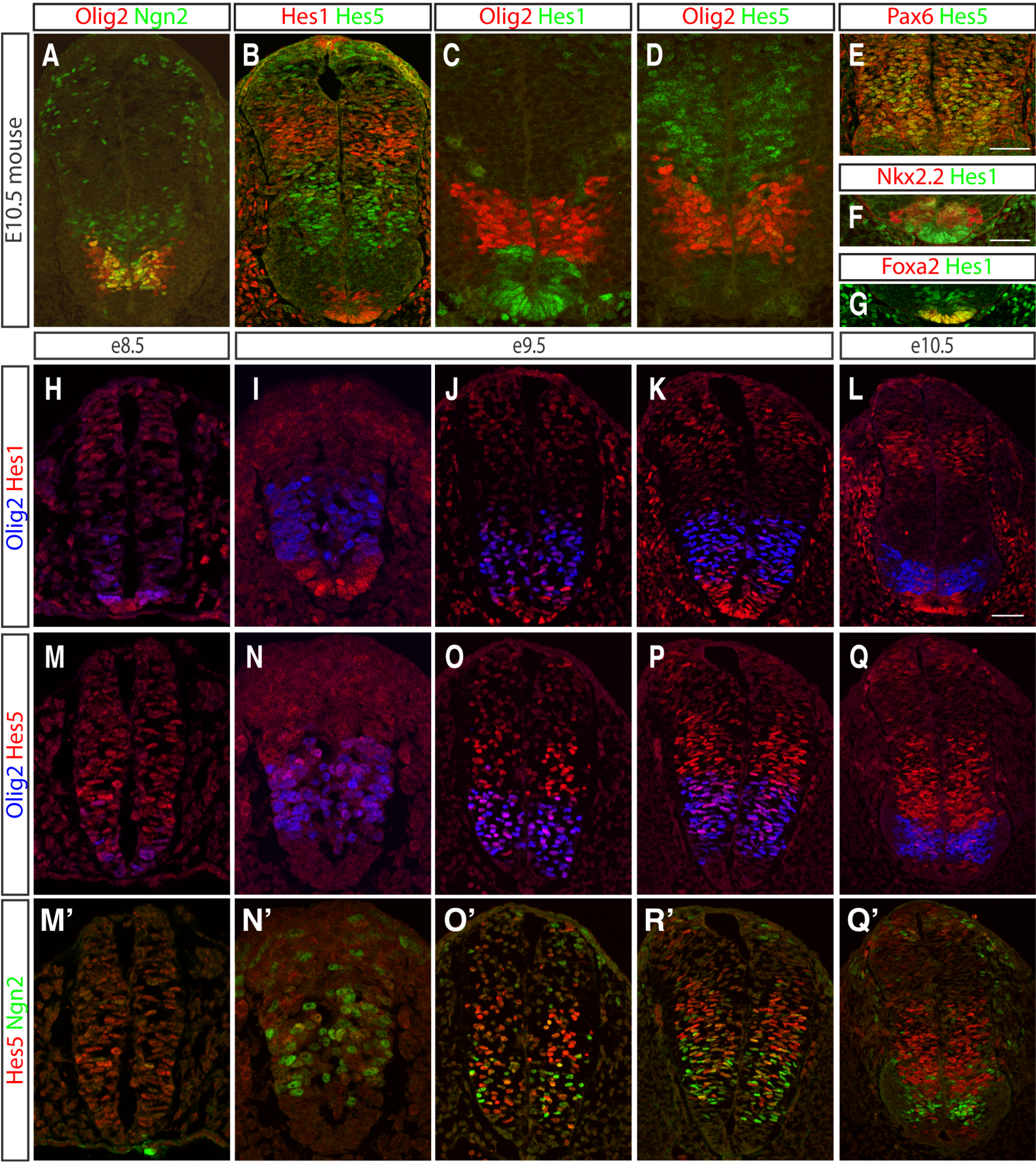
Olig2 Ngn2
Hes1 Hes5
Olig2 Hes1
Olig2 Hes5
Pax6 Hes5
E10.5 mouse
A
B
C
D
E
Nkx2.2 Hes1
F
Foxa2 Hes1
G
e8.5
e9.5
e10.5
Olig2 Hes1
H
I
J
K
L
Olig2 Hes5
M
N
O
P
Q
Hes5 Ngn2
M'
N'
O'
R'
Q'

Sagner et al. - Figure 6

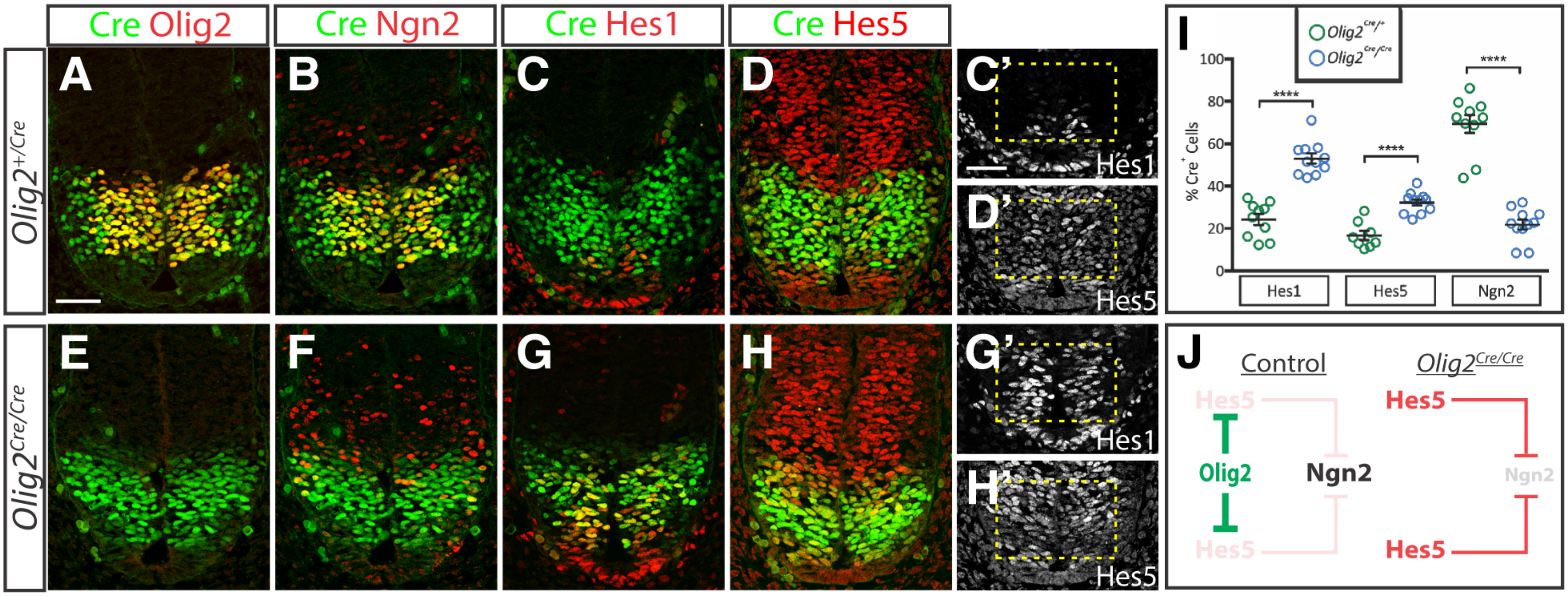
Cre Olig2
Cre Ngn2
Cre Hes1
Cre Hes5
$Olig2^{+/Cre}$
A
B
C
D
C'
Hes1
D'
Hes5
$Olig2^{Cre/Cre}$
E
F
G
H
G'
Hes1
H'
Hes5
I
$Olig2^{Cre/+}$
$Olig2^{Cre/Cre}$
% Cre+ Cells
100
80
60
40
20
0
****
****
****
Hes1
Hes5
Ngn2
J
Control
$Olig2^{Cre/Cre}$
Hes5
Olig2
Ngn2
Hes5
Hes5
Ngn2
Hes5

Sagner et al. - Figure 7

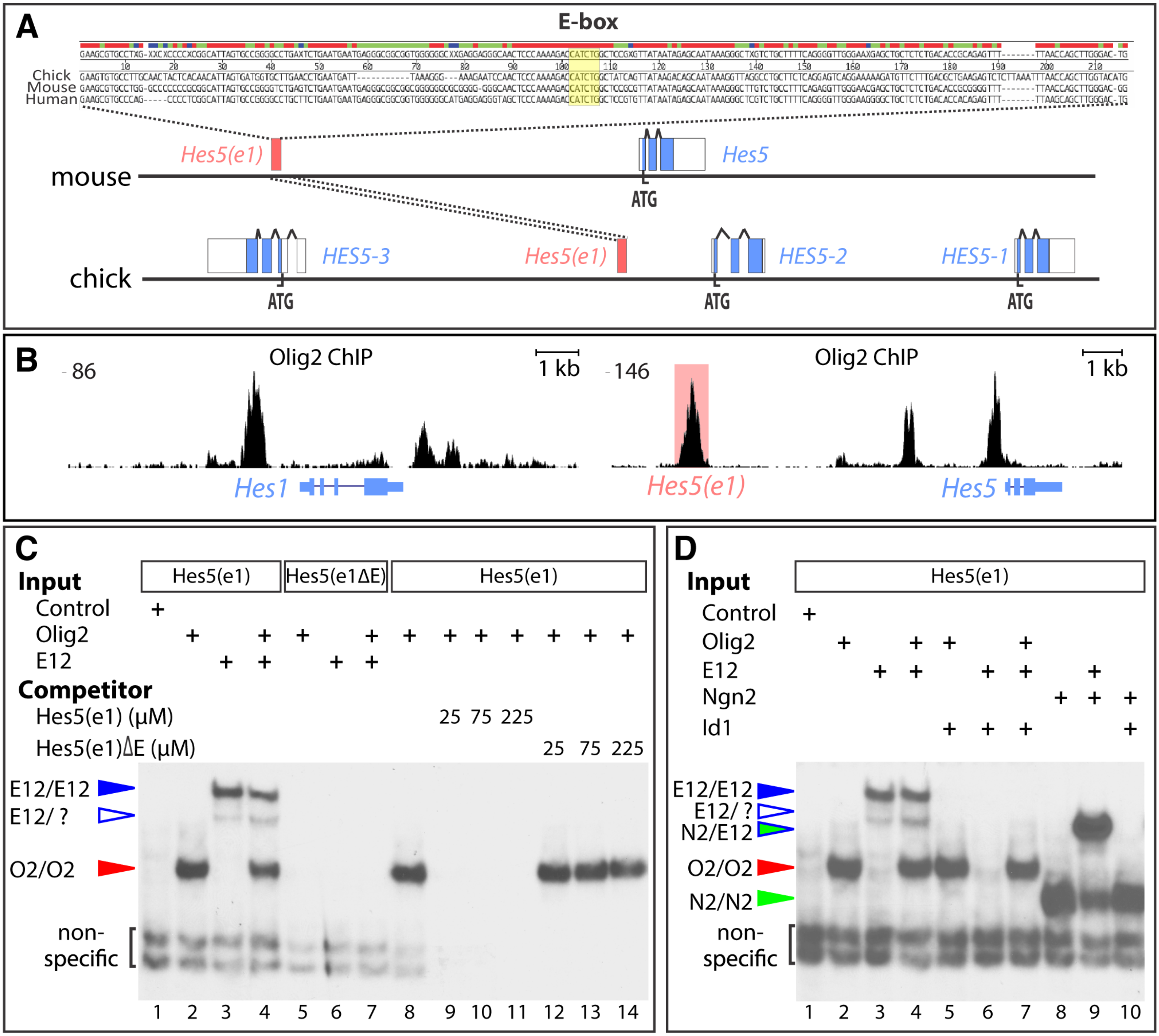
A
E-box
10
20
30
40
50
60
70
80
90
100
110
120
130
140
150
160
170
180
190
200
210
Chick
Mouse
Human
Hes5(e1)
Hes5
mouse
ATG
HES5-3
Hes5(e1)
HES5-2
HES5-1
chick
ATG
ATG
ATG
B
86
Olig2 ChIP
1 kb
146
Olig2 ChIP
1 kb
Hes1
Hes5(e1)
Hes5
C
Input
Hes5(e1)
Hes5(e1ΔE)
Hes5(e1)
Control
Olig2
E12
Competitor
Hes5(e1) (µM)
25 75 225
Hes5(e1)ΔE (µM)
25 75 225
E12/E12
E12/ ?
O2/O2
non-specific
1 2 3 4 5 6 7 8 9 10 11 12 13 14
D
Input
Hes5(e1)
Control
Olig2
E12
Ngn2
Id1
E12/E12
E12/ ?
N2/E12
O2/O2
N2/N2
non-specific
1 2 3 4 5 6 7 8 9 10

Sagner et al. - Figure 8

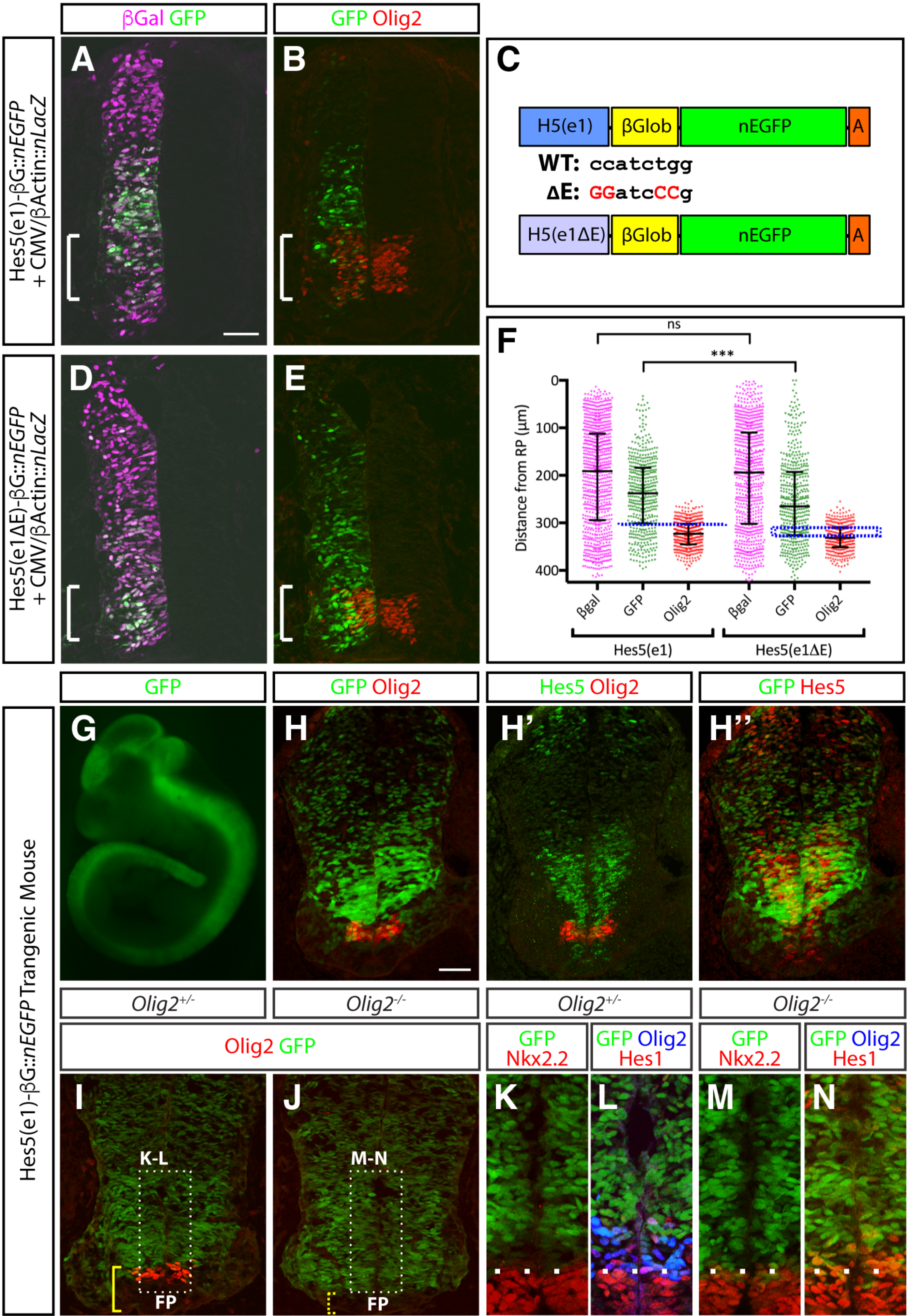
βGal GFP
GFP Olig2
Hes5(e1)-βG::nEGFP + CMV/βActin::nLacZ
A
B
C
H5(e1)
βGlob
nEGFP
A
WT: ccatctgg
ΔE: GGatcCCg
H5(e1ΔE)
βGlob
nEGFP
A
Hes5(e1ΔE)-βG::nEGFP + CMV/βActin::nLacZ
D
E
F
ns
***
Distance from RP (µm)
0
100
200
300
400
βgal
GFP
Olig2
βgal
GFP
Olig2
Hes5(e1)
Hes5(e1ΔE)
GFP
GFP Olig2
Hes5 Olig2
GFP Hes5
G
H
H'
H''
Hes5(e1)-βG::nEGFP Trangenic Mouse
Olig2+/-
Olig2-/-
Olig2+/-
Olig2-/-
Olig2 GFP
GFP Nkx2.2
GFP Olig2 Hes1
GFP Nkx2.2
GFP Olig2 Hes1
I
J
K
L
M
N
K-L
M-N
FP
FP

Sagner et al. - Figure 1-figure supplement 1

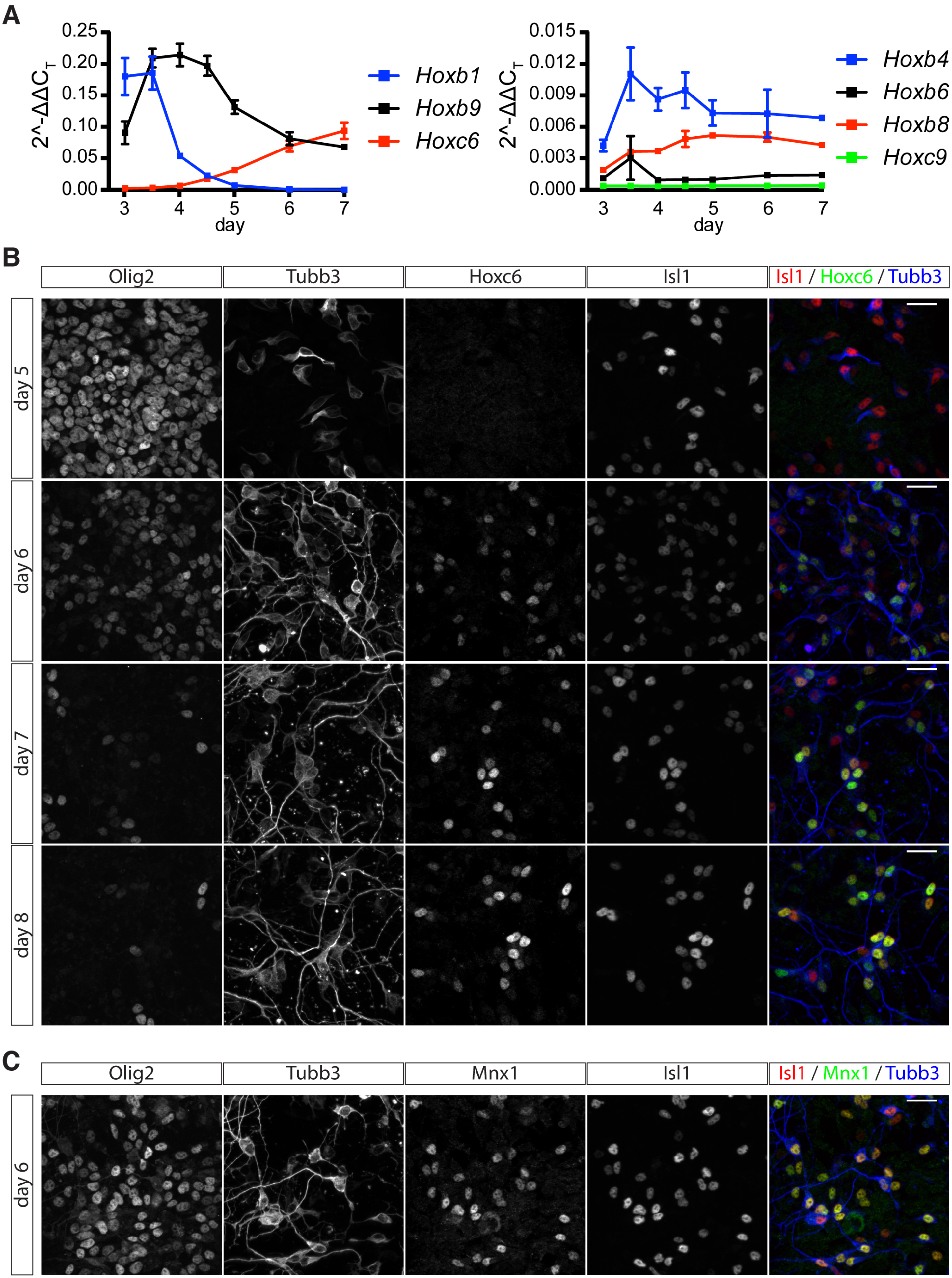

Sagner et al. - Figure 2-figure supplement 1

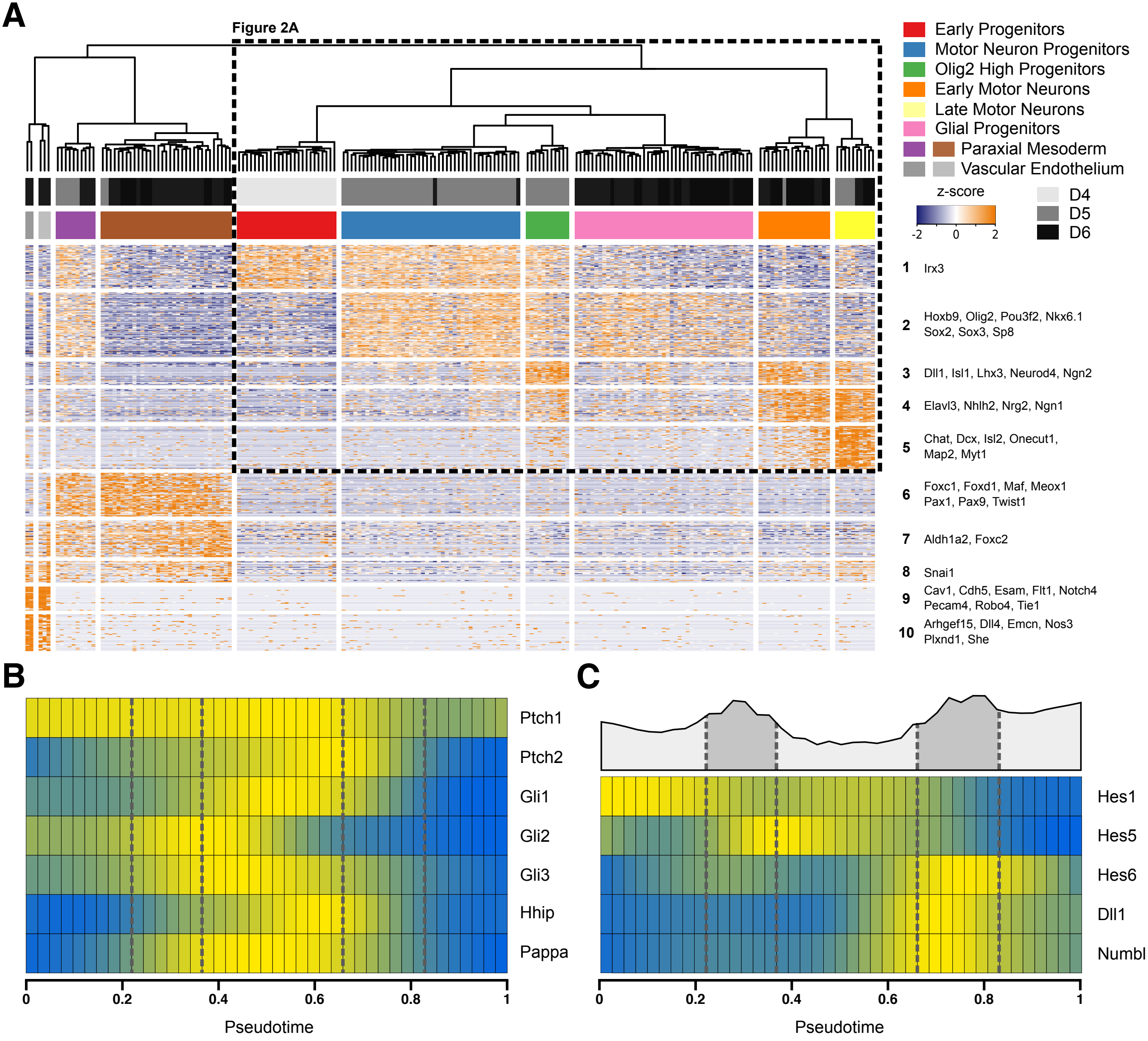

Sagner et al. - Figure 3-figure supplement 1

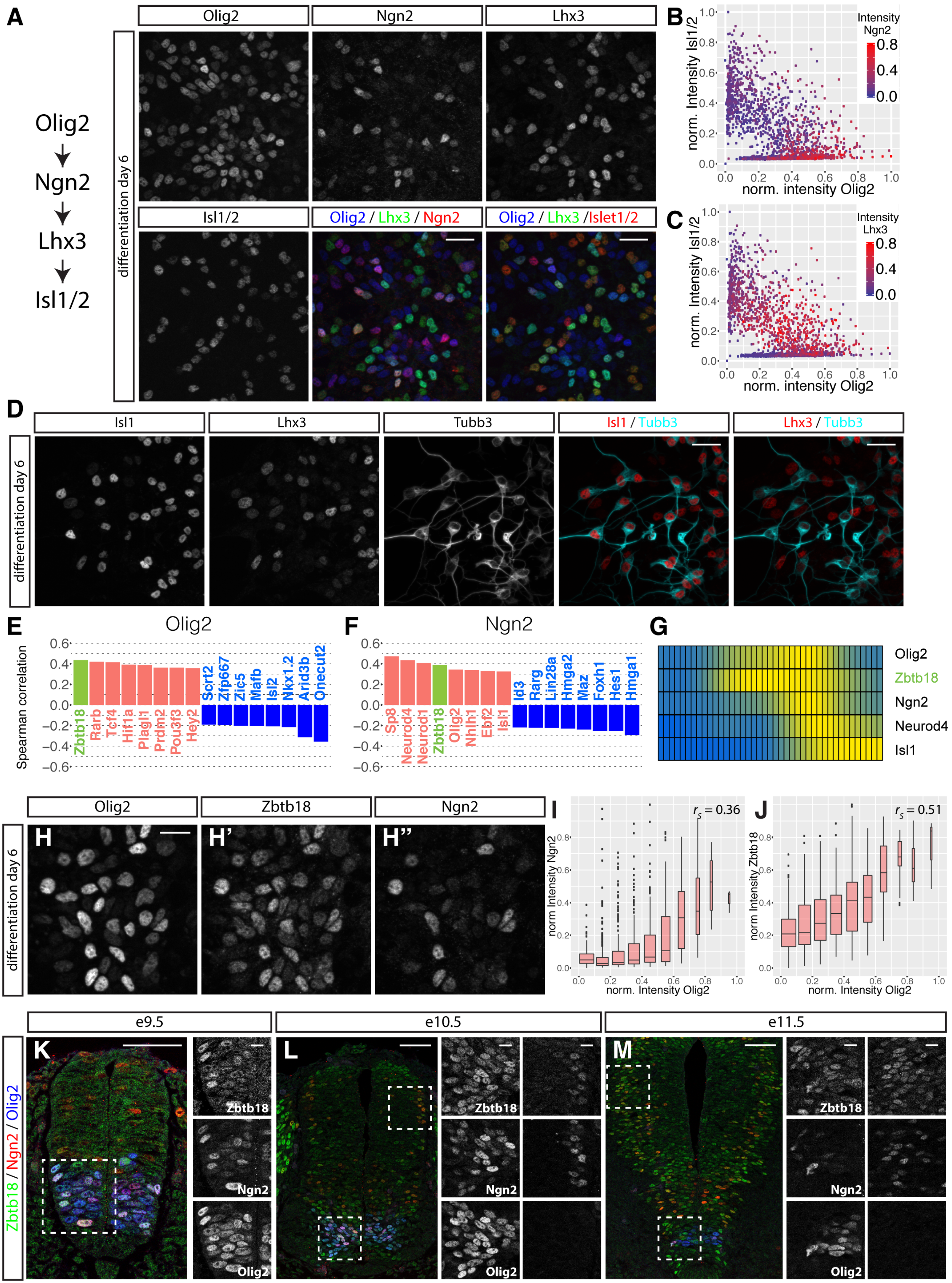
A
Olig2
Ngn2
Lhx3
Isl1/2
Olig2 / Lhx3 / Ngn2
Olig2 / Lhx3 /Islet1/2
differentiation day 6
Olig2 → Ngn2 → Lhx3 → Isl1/2
B
norm. Intensity Isl1/2
norm. intensity Olig2
Intensity Ngn2
0.8
0.4
0.0
0.0 0.2 0.4 0.6 0.8 1.0
C
norm. Intensity Isl1/2
norm. intensity Olig2
Intensity Lhx3
0.8
0.4
0.0
D
Isl1
Lhx3
Tubb3
Isl1 / Tubb3
Lhx3 / Tubb3
differentiation day 6
E
Olig2
Spearman correlation
0.6 0.4 0.2 0.0 −0.2 −0.4 −0.6
Zbtb18
Rarb
Tcf4
Hif1a
Plagl1
Prdm2
Pou3f3
Hey2
Scrt2
Zfp667
Zic5
Mafb
Isl2
Nkx1.2
Arid3b
Onecut2
F
Ngn2
Sp8
Neurod4
Neurod1
Zbtb18
Olig2
Nhlh1
Ebf2
Isl1
Id3
Rarg
Lin28a
Hmga2
Maz
Foxh1
Hes1
Hmga1
G
Olig2
Zbtb18
Ngn2
Neurod4
Isl1
Olig2
Zbtb18
Ngn2
H
H'
H''
differentiation day 6
I
r_s = 0.36
norm Intensity Ngn2
norm. Intensity Olig2
J
r_s = 0.51
norm Intensity Zbtb18
norm. Intensity Olig2
e9.5
e10.5
e11.5
K
L
M
Zbtb18 / Ngn2 / Olig2
Zbtb18
Ngn2
Olig2

Sagner et al. - Figure 4-figure supplement 1

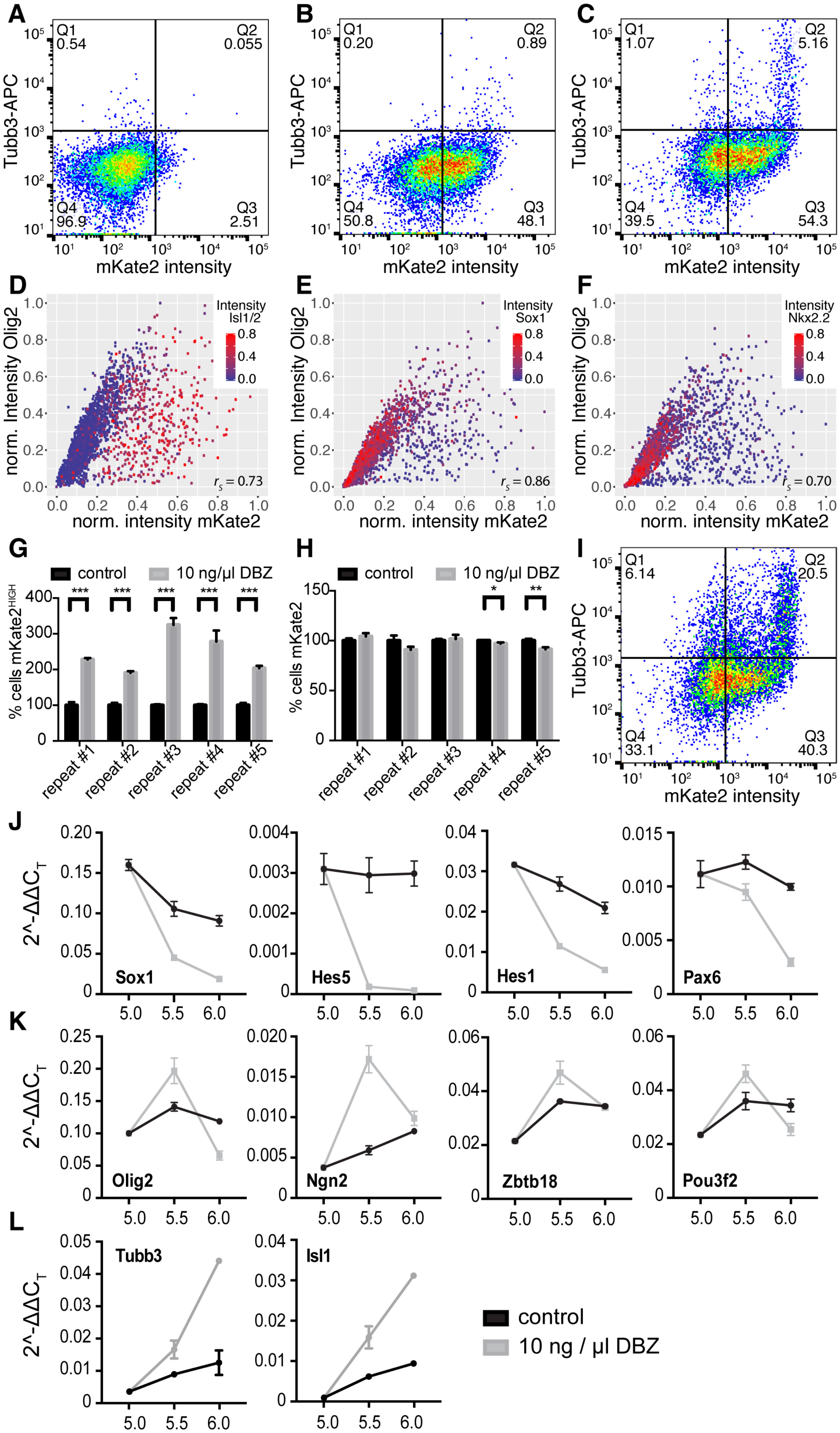

Sagner et al. - Figure 6-figure supplement 1

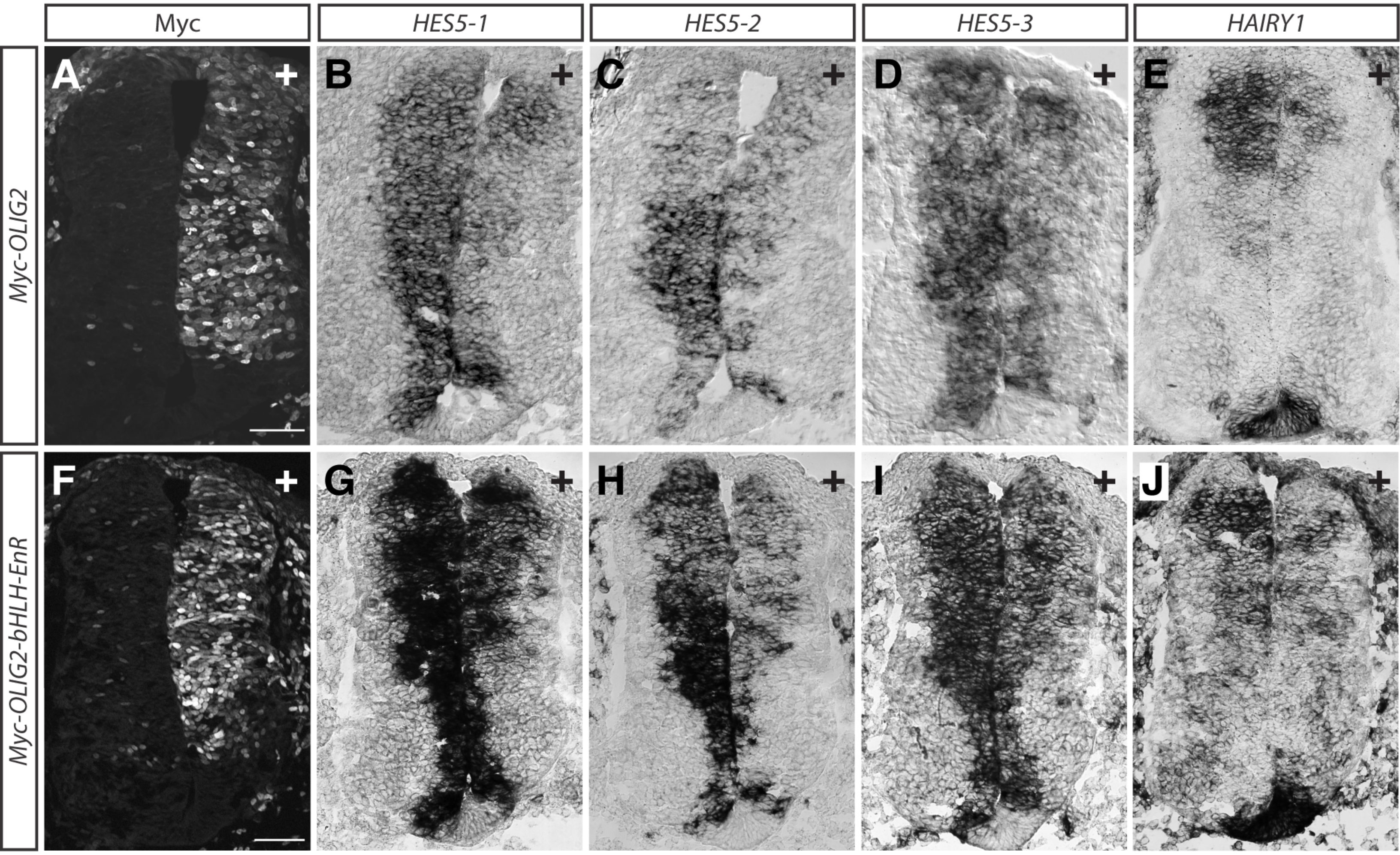
Myc
HES5-1
HES5-2
HES5-3
HAIRY1
Myc-OLIG2
Myc-OLIG2-bHLH-EnR
A
+
B
+
C
+
D
+
E
+
F
+
G
+
H
+
I
+
J
+

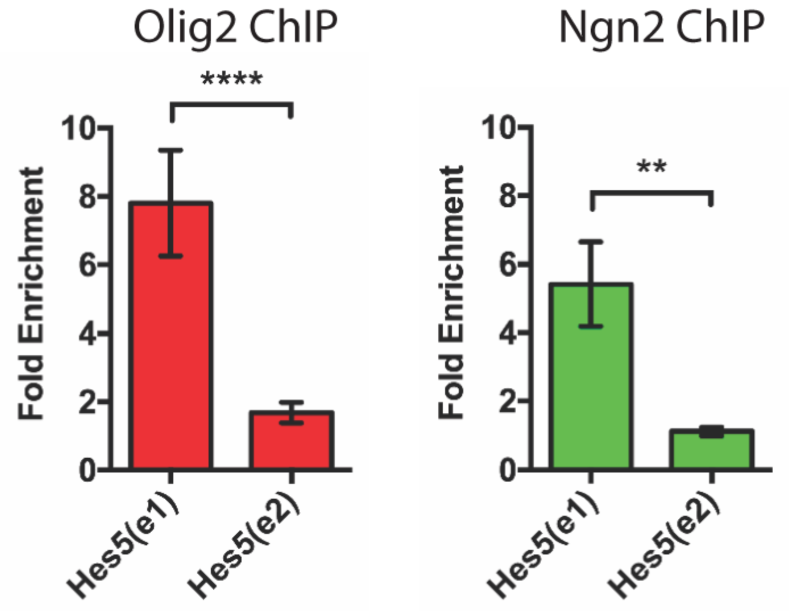Sagner et al. - Figure 7-figure supplement 1